

# Carbon and hydrogen radio recombination lines from the cold clouds towards Cassiopeia A

J. B. R. Oonk,<sup>1,2★</sup> R. J. van Weeren,<sup>3</sup> P. Salas,<sup>1</sup> F. Salgado,<sup>1</sup> L. K. Morabito,<sup>1</sup>  
M. C. Toribio,<sup>1</sup> A. G. G. M. Tielens<sup>1</sup> and H. J. A. Röttgering<sup>1</sup>

<sup>1</sup>*Leiden Observatory, Leiden University, PO Box 9513, NL-2300 RA Leiden, the Netherlands*

<sup>2</sup>*Netherlands Institute for Radio Astronomy (ASTRON), Postbus 2, NL-7990 AA Dwingeloo, the Netherlands*

<sup>3</sup>*Harvard-Smithsonian Center for Astrophysics, 60 Garden Street, Cambridge, MA 02138, USA*

Accepted 2016 October 31. Received 2016 October 26; in original form 2016 August 14

## ABSTRACT

We use the Low Frequency Array to perform a systematic high spectral resolution investigation of the low-frequency 33–78 MHz spectrum along the line of sight to Cassiopeia A. We complement this with a 304–386 MHz Westerbork Synthesis Radio Telescope observation. In this first paper, we focus on the carbon radio recombination lines. We detect Cn $\alpha$  lines at  $-47$  and  $-38$  km s $^{-1}$  in absorption for quantum numbers  $n = 438$ – $584$  and in emission for  $n = 257$ – $278$  with a high signal-to-noise ratio. These lines are associated with cold clouds in the Perseus spiral arm component. Hn $\alpha$  lines are detected in emission for  $n = 257$ – $278$ . In addition, we also detect Cn $\alpha$  lines at  $0$  km s $^{-1}$  associated with the Orion arm. We analyse the optical depth of these transitions and their linewidth. Our models show that the carbon line components in the Perseus arm are best fitted with an electron temperature of  $85$  K and an electron density of  $0.04$  cm $^{-3}$  and can be constrained to within 15 per cent. The electron pressure is constrained to within 20 per cent. We argue that most of these carbon radio recombination lines arise in the CO-dark surface layers of molecular clouds, where most of the carbon is ionized, but hydrogen has made the transition from atomic to molecular. The hydrogen lines are clearly associated with the carbon line emitting clouds, but the low-frequency upper limits indicate that they likely do not trace the same gas. Combining the hydrogen and carbon results, we arrive at a firm lower limit to the cosmic-ray ionization rate of  $2.5 \times 10^{-18}$  s $^{-1}$ , but the actual value is likely much larger.

**Key words:** ISM: clouds – ISM: individual objects: Cassiopeia A – radio lines: ISM.

## 1 INTRODUCTION

Spectral lines resulting from atoms recombining with electrons in diffuse, ionized plasma are potentially important diagnostics to probe the conditions of the emitting and absorbing gas. At low quantum numbers, recombination gives rise to the well-known optical and near-infrared recombination lines. At higher quantum numbers, the energy spacing between subsequent quantum levels decreases and a recombination line transition will emit a photon at radio wavelengths. The associated lines for high quantum numbers are therefore called radio recombination lines (RRLs).

RRLs can be used to obtain a wealth of information on the properties of the emitting gas (e.g. Gordon & Soroichenko 2009). Emitting in the radio domain, these lines are unbiased by dust obscuration. At low radio frequencies ( $<1$  GHz), RRLs provide us with a method to obtain the temperature, density and ionization of the cold

neutral medium (CNM; e.g. Shaver 1975, 1976a,b; Soroichenko & Smirnov 1987; Payne, Anantharamaiah & Erickson 1989; Oonk et al. 2015). This information cannot easily be obtained by other means such as 21-cm neutral hydrogen measurements.

Our own Galaxy is a copious emitter of RRLs. These come in two flavours: (i) warm, dense gas RRLs (sometimes, in the literature, referred to as classical or discrete RRLs), and (ii) diffuse RRLs. Warm, dense gas RRLs are associated with common H II regions and dense photodissociation regions (PDRs). Here, recombination lines from hydrogen, helium and carbon are seen (e.g. Palmer 1967; Roelfsema, Goss & Geballe 1989; Natta, Walmsley & Tielens 1994; Wyrowski et al. 1997; Kantharia, Anantharamaiah & Goss 1998b; Konovalenko & Stepkin 2005). These are predominantly observed at frequencies above 1 GHz as the hydrogen and helium recombination lines trace the warm ( $T_e \sim 10^4$  K), high-density ( $n_e > 10$  cm $^{-3}$ ) fully ionized gas, whereas the carbon recombination lines trace the warm ( $\sim 500$  K), dense ( $n_H \sim 10^3$ – $10^6$  cm $^{-3}$ ) gas in PDRs bordering compact H II regions or associated with reflection nebulae.

\* E-mail: oonk@strw.leidenuniv.nl

Diffuse RRLs are associated with the lower density, colder interstellar medium (ISM; e.g. Blake et al. 1980; Konovalenko & Sodin 1980; Payne et al. 1989; Golynkin & Konovalenko 1991a,b; Erickson, McConnell & Anantharamaiah 1995; Kantharia & Anantharamaiah 2001; Oonk et al. 2014, 2015; Salgado et al. 2016a,b). Here, typically, only recombination lines from carbon (CRRLs) are observed as the ionization levels are too low to produce observable hydrogen and helium lines. Diffuse CRRLs are best observed at radio frequencies below 1 GHz due to stimulated emission and absorption. Whereas warm, dense gas RRLs have been studied in great detail, the properties of the cold gas associated with diffuse RRLs in our Galaxy are not well determined. Furthermore, these diffuse RRLs provide us with a complementary tracer of the physical conditions in the CNM of the Milky Way.

So far, the only line of sight studied in some detail for CRRLs is the one towards the bright supernova remnant Cassiopeia A (Cas A). This is because Cas A is one of the brightest low-frequency radio sources in the sky (e.g. Baars, Mezger & Wendker 1965; Bridle & Purton 1968; Parker 1968), thus serving as a dominating background source, and it shows relatively bright CRRLs in both emission and absorption (e.g. Payne et al. 1989). The sightline towards Cas A cuts through the Milky Way at a galactic longitude  $l = 112^\circ$  and latitude  $b = -2^\circ$ . Cas A itself is located in the second Galactic quadrant in the Perseus spiral arm at a distance of 3.4 kpc from the Sun and at a Galactocentric radius of about 10.5 kpc. H I 21-cm line observations show both emission and absorption in the range of +30 to  $-120 \text{ km s}^{-1}$  (e.g. Mebold & Hills 1975; Bieging, Goss & Wilcots 1991; Schwarz, Goss & Kalberla 1997). The strongest H I absorption features are found around  $-47$ ,  $-38$  and  $0 \text{ km s}^{-1}$ . These are associated with foreground clouds in the Perseus ( $-47$  and  $-38 \text{ km s}^{-1}$ ) arm and the Orion ( $0 \text{ km s}^{-1}$ ) spur. These clouds are also observed in other cold gas tracers such as C I (492 GHz), CO ( $J = 2-1$ ), OH, H<sub>2</sub>CO and NH<sub>3</sub> (e.g. de Jager et al. 1978; Batrla, Wilson & Martin-Pintado 1983; Batrla, Walmsley & Wilson 1984; Anantharamaiah et al. 1994; Liszt & Lucas 1999; Mookerjee et al. 2006; Kilpatrick, Bieging & Rieke 2014).

The CRRLs along this line of sight have been studied by, e.g. Payne et al. (1989), Anantharamaiah et al. (1994), Kantharia, Anantharamaiah & Payne (1998a), Gordon & Sorochenko (2009) and Asgekar et al. (2013). It was found that the CRRLs show a good correspondence with H I 21-cm absorption, both in velocity and in distribution, and somewhat less good with CO ( $J = 2-1$ ) emission. Attempts were made at modelling the CRRL properties as a function of quantum number  $n$  to derive the physical parameters of the CRRL-emitting gas (e.g. Payne et al. 1989; Kantharia et al. 1998a). These investigations showed that the velocity-averaged CRRLs from the Perseus arm favour warmer, lower density models (electron temperature  $T_e \sim 75 \text{ K}$  and electron density  $n_e \sim 0.02 \text{ cm}^{-3}$ ) over colder and denser models ( $T_e \sim 30 \text{ K}$  and  $n_e \sim 0.05$ ). However, a clear discrimination was not possible, as the models presented by Payne et al. (1989) and Kantharia et al. (1998a) were not able to simultaneously fit the  $>150 \text{ MHz}$  CRRL emission in combination with the  $<150 \text{ MHz}$  CRRL absorption. Furthermore, the results they obtain from the linewidths differed from those obtained from the optical depths. This is likely due to a number of factors: (i) the limited validity of the CRRL models used at the time; (ii) the difficulty in determining the total line profile at low frequencies; and (iii) averaging over multiple velocity components with potentially different physical gas conditions.

Here, we revisit the Cas A CRRL line of sight making use of new high-quality, high spectral resolution interferometric data from the Low Frequency Array (LOFAR; van Haarlem et al. 2013) and

the Westerbork Synthesis Radio Telescope (WSRT) to perform a velocity-resolved study of the CRRLs. In addition, we make use of our new CRRL models (Salgado et al. 2016a,b) to derive the physical conditions of the associated gas.

The data presented in this paper are part of the LOFAR Cas A Spectral Survey (LCASS). This ongoing survey is a dedicated (Directors Discretionary Time) programme aimed at performing the first detailed low-frequency, high-spectral-resolution, interferometric LOFAR study of the cold ISM along the well-studied Cas A line of sight. The survey, when complete, will cover the entire frequency range accessible to LOFAR, i.e. 10–80, 110–190 and 200–250 MHz, with a velocity resolution ranging from  $11 \text{ km s}^{-1}$  at the lowest frequency to  $1 \text{ km s}^{-1}$  at the highest frequency. The primary goal of LCASS is to provide a high signal-to-noise ratio spectral line atlas and spatial maps of low-frequency CRRLs. In addition, we will also search the low-frequency spectrum for line emission and absorption from other atoms and molecules (e.g. OH and NO). The search for non-RRL lines will be presented in a future paper. In this paper, we present the LCASS RRL results for the 33–78 MHz range.

This paper is structured as follows. In Section 2, we discuss the first LOFAR observations taken for the LCASS survey and the WSRT observations. The results are presented in Section 3. In Section 4, we fit our new CRRL models to the observations. We discuss the results in Section 5 and present our conclusions in Section 6.

## 2 OBSERVATIONS AND REDUCTION

### 2.1 LOFAR (33–78 MHz)

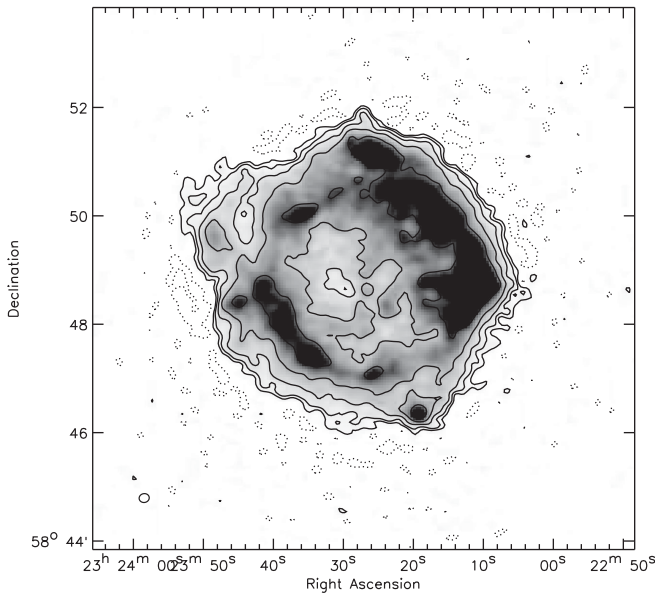
We obtained LOFAR LBA observations on 2011 December 27 from 10:00 to 20:30 UTC and on 2013 October 31 from 11:55 to 21:55 UTC (Table 1). For each of these observations, LOFAR’s multibeaming capabilities were used to place half of the available instantaneous bandwidth on Cas A, 122 subbands each 0.1953 MHz wide, totalling about 24 MHz. The other 122 subbands were pointed towards Cyg A, which served as a calibrator (Oonk et al. 2014). For both pointing centres, we obtained complete frequency coverage between 33–57 MHz (2011) and 55–78 MHz (2013), although about 24 subbands were corrupted due to issues with the LOFAR offline storage system. The LBA\_OUTER configuration was used for the LBA stations. In this case, 48 (of 96) LBA antennas are used, located mostly in the outer part of the 87-m-diameter stations. All four linear correlation products were recorded (XX, XY, YX, YY), and each subband was subdivided into 512 frequency channels. The integration time was 2 s.

For the 2011 observation, we used 9 remote and 22 core stations providing baselines between 90 m and 80 km. A first step in the data processing is the automatic flagging of radio frequency interference (RFI) with the AOFlagger (Offringa et al. 2010). We slightly decreased the default flagging thresholds to avoid flagging good data as Cas A and Cyg A have flux densities  $>10^4 \text{ Jy}$  in the observed frequency range. Typically, a few per cent of the data were flagged due to RFI. After flagging, we averaged the data to 4 s time-steps to reduce its size. The data were calibrated with the BlackBoard Selfcal (BBS) software system (Pandey et al. 2009). We used high-resolution 10-arcsec clean components models of Cas A (Fig. 1) and Cyg A (McKean et al., 2016) for calibration. These models were obtained from previous LOFAR observations around 70 MHz.

As the observations are pointed towards the two brightest sources on the sky, either Cas A or Cyg A dominates the total signal on all baselines. We made a copy of the 4-s data and averaged further down

**Table 1.** Details of the observations. Note that for WSRT, we cycle through  $6 \times 8$  spectral setups in time so that the on-source time per line amounts to about 1.5 h.

Parameter	LOFAR LBA (1)	LOFAR LBA (2)	WSRT <i>P</i> band
Data ID	L40787	L184343	S12A/002
Field centre RA (J2000)	23 <sup>h</sup> 23 <sup>m</sup> 22 <sup>s</sup> .8	23 <sup>h</sup> 23 <sup>m</sup> 22 <sup>s</sup> .8	23 <sup>h</sup> 23 <sup>m</sup> 27 <sup>s</sup> .9
Field centre Dec. (J2000)	+58 <sup>d</sup> 50 <sup>m</sup> 16 <sup>s</sup>	+58 <sup>d</sup> 50 <sup>m</sup> 16 <sup>s</sup>	+58 <sup>d</sup> 48 <sup>m</sup> 42 <sup>s</sup>
Observing date	2011 December 27	2013 October 31	2012 January 28
Total on-source time	10.5 h	10 h	12 h
Frequency range	33–57 MHz	55–78 MHz	300–390 MHz
Number of subbands	122	122	6
Width of a subband	0.195 MHz	0.195 MHz	1.25 MHz
Channels per subband	512	512	2048
Channel width	2.0–3.5 km s <sup>−1</sup>	1.5–2.1 km s <sup>−1</sup>	0.5–1.0 km s <sup>−1</sup>

**Figure 1.** Cas A continuum image at 69 MHz obtained from a single 0.2-MHz subband. This image was made from a LOFAR LBA observation, taken on 2011 October 15, using uniform weighting and has a resolution of  $11.2 \times 9.8$  arcsec<sup>2</sup>.

from 512 to 1 channel per subband. We then obtained gain solutions for all four correlations with *BBS* on a 4 s time-scale. We assume that the sources are unpolarized over the observed frequency range. The gain solutions found were then applied to the 512 frequency channel data, and a final round of flagging was carried out with the *AOFlagger*. Channel cubes were made with *CASAPY*, imaging and cleaning each channel individually. The first 25 and last 25 channels of the data were ignored as they are too noisy. We chose Briggs weighting (Briggs 1995) with a robust value of 0.5 to create images with a resolution ranging between  $30 \times 40$  and  $40 \times 60$  arcsec<sup>2</sup>. We then convolved all images from all subbands to a common resolution of  $45 \times 65$  arcsec<sup>2</sup> and created an image cube for each subband.

For the 2013 observation, we used 24 core stations and 14 remote stations. The data reduction was performed in the same way as for the 2011 data set. Due to a clock problem, only 18 core stations were used in the final analysis of the observations. We chose Briggs weighting with a robust value of 0.5 to create images with a resolution ranging between  $215 \times 255$  and  $310 \times 360$  arcsec<sup>2</sup>, the lower resolution being a consequence of using only 18 core stations. We then convolved all images from all subbands to a common

resolution of  $350 \times 400$  arcsec<sup>2</sup> and created an image cube for each subband.

## 2.2 WSRT (304–386 MHz)

We obtained WSRT *P*-band observations on 2012 January 28 from 08:29 to 20:28 UTC (Table 1). The observations were carried out in the Maxi-short configuration and Doppler tracking was turned off. We observed in frequency-switching mode with 10-s sampling and six simultaneous 1.25-MHz subbands (IVC bands) each having 2048 channels (using recirculation) and 2 polarizations (XX,YY). Each subband is centred near an expected CRRL frequency, and we observe three CRRLs per setup, where each line is covered twice with a different central frequency setting (typically offset by 0.3–0.4 MHz). In total, we specified 8 spectral setups of 6 subbands and covered a total of 24 lines (all  $22\alpha$  lines within the observed frequency range and 2 additional  $\beta$  lines). Each spectral setup was observed for 10 min on source and then changed to the next setup, and after the last setup was done, we returned to the first setup. This way we cycled the spectral setups through the full 12-h observation and created similar ultraviolet (UV) and time coverage for each subband. The total observing time per subband was about 1.5 h.

The first step in the data reduction was the automatic flagging of RFI with the *AOFlagger*. A dedicated WSRT *P*-band flagging strategy was developed for this purpose. The data were then averaged down and calibrated with *CASA* (McMullin et al. 2007) using the high-resolution 10 arcsec clean components model of Cas A (Fig. 1). Gain solutions were obtained for both polarizations on a 10 s time-scale. The gain solutions found were then applied to the 2048 frequency channel data, and a final round of flagging was carried out with the *AOFlagger*. Channel cubes were made with *CASAPY*, imaging and cleaning each channel individually. We chose Briggs weighting (Briggs 1995) with a robust value of 0.5 to create images with a resolution ranging between  $60 \times 65$  and  $75 \times 95$  arcsec<sup>2</sup>. We then convolved all images from all subbands to a common resolution of  $80 \times 100$  arcsec<sup>2</sup> and created an image cube for each subband.

## 2.3 Spectral analysis and line stacking

From the WSRT 300–390 MHz and LBA 33–57 MHz image cubes, we extracted spatially integrated on-source spectra from an  $8 \times 8$  arcmin<sup>2</sup> aperture centred on Cas A. For the LBA 55–78 MHz range, we used a  $14 \times 14$  arcmin<sup>2</sup> aperture centred on Cas A. The larger aperture for the 55–78 MHz data is necessary, given the lower spatial resolution of this observation. The CRRL  $\alpha$  ( $\Delta n = 1$ ) lines are clearly visible in the individual spectra for both LOFAR

**Table 2.** Individual  $\alpha$  line transitions included in each CRRL and HRRL line stack.

Stack ( $n$ )	Species	Individual $\alpha$ line transitions ( $n$ )	Observation
260	C and H	257, 258, 260, 261, 262	WSRT
266	C and H	263, 264, 265, 267, 268	WSRT
271	C and H	270, 271, 272, 273	WSRT
276	C and H	274, 275, 276, 277, 278	WSRT
438	C	435, 436, 437, 438, 439, 440, 442	LBA (2)
448	C	443, 444, 445, 447, 449, 452, 454	LBA (2)
459	C	456, 457, 459, 460, 461, 463	LBA (2)
467	C	464, 465, 466, 467, 468, 472	LBA (2)
477	C	473, 474, 475, 479, 480, 481	LBA (2)
485	C	482, 483, 484, 486, 487, 488, 489	LBA (2)
496	C	491, 492, 493, 495, 496, 497, 498, 499, 500, 501, 503, 504, 505	LBA (1)
510	C	506, 507, 508, 509, 510, 511, 512, 513, 514, 515, 517, 518, 519	LBA (1)
527	C	522, 523, 525, 526, 528, 529, 530, 531, 532, 533, 534, 535	LBA (1)
542	C	536, 537, 538, 540, 541, 542, 543, 544, 547, 548, 549, 550	LBA (1)
559	C	551, 552, 553, 554, 558, 559, 560, 561, 562, 563, 565, 566	LBA (1)
575	C	567, 568, 569, 573, 574, 575, 576, 577, 578, 579, 580, 581, 584	LBA (1)
439	H	435, 436, 437, 438, 439, 440, 441, 442	LBA (2)
447	H	443, 445, 446, 447, 448, 449, 450, 451	LBA (2)
458	H	454, 455, 456, 457, 458, 459, 460, 461	LBA (2)
466	H	462, 463, 464, 465, 466, 469, 470, 471	LBA (2)
475	H	472, 473, 474, 475, 476, 477, 478	LBA (2)
485	H	481, 482, 483, 484, 485, 487, 488, 489	LBA (2)
496	H	491, 492, 493, 495, 496, 498, 499, 501, 502, 503, 504, 505	LBA (1)
510	H	506, 507, 508, 509, 510, 511, 512, 513, 514, 515, 516, 517	LBA (1)
527	H	519, 522, 523, 525, 526, 528, 529, 531, 532, 533, 535, 536	LBA (1)
542	H	537, 538, 540, 541, 542, 543, 544, 546, 547, 548, 549, 550	LBA (1)
559	H	551, 552, 556, 557, 558, 559, 560, 561, 562, 563, 565, 566	LBA (1)
575	H	567, 568, 569, 574, 575, 576, 577, 578, 579, 580, 581, 582, 584	LBA (1)

and WSRT. We investigated the overlapping subbands containing CRRLs between the two LOFAR observations and found that the line profile parameters agreed within errors.

We removed the edge channels from the spectra and fitted a low-order polynomial to the line-free channels to estimate the continuum. We then convert the spectra to optical depth units following Oonk et al. (2014). The typical spectral rms per channel, in optical depth units, are  $5 \times 10^{-4}$ ,  $6 \times 10^{-4}$  and  $4 \times 10^{-4}$  for LOFAR 55–78 MHz, 33–57 MHz and WSRT, respectively. The peak signal-to-noise ratio for individual  $\alpha$  lines in the LOFAR spectra is typically 7–9 for the  $-47$  component and 2–4 for the  $-38$  km s $^{-1}$  component. Similarly, for WSRT, the typical peak signal-to-noise ratio is about 5 for the  $-47$  and 1.5 for the  $-38$  component.

We perform line spectra stacking to obtain higher signal-to-noise ratio line profiles necessary to measure the line optical depth and line full width at half-maximum (FWHM) of each of the velocity components. The initial stacking of line spectra was performed as described in Oonk et al. (2014). These stacked spectra contain, on average, 6 $\alpha$  lines in the WSRT range and 10–20 stacked lines in the LBA range (Table 2). Stacking these lines over small changes in  $n$  is allowed as we expect the RRLs to change slowly and smoothly in the observed frequency ranges.

The stacked WSRT spectra are shown in Fig. 2, and the line profiles are found to be Gaussian. The three velocity components at  $-47$ ,  $-38$  and  $0$  km s $^{-1}$  are narrow enough and sufficiently separated that we can fit them well with individual Gaussians. There is an additional line feature at  $-55$  km s $^{-1}$ , likely due to RRLs from sulphur, which we blank prior to fitting the CRRLs. The results from the Gaussian fits are summarized in Table 3. A stacked spectrum containing all  $\alpha$  lines in the WSRT range is shown in Fig. 3. For this stacked spectrum, we also fit the  $-55$  km s $^{-1}$  feature after

subtracting the CRRL fits from the spectrum. The results from the Gaussian fits to this stacked spectrum are summarized in Table 4. This latter spectrum is used only for our investigation of the gas ionization using the hydrogen lines in Section 5.2.

For the LBA spectra, there is strong line broadening with decreasing frequency, as expected from the Stark effect (e.g. Section 4.1). This leads to significant line blending for the  $-47$  and  $-38$  km s $^{-1}$  components. Furthermore, this causes the line profiles to have Voigt profiles instead of Gaussian profiles. Voigt profiles are characterized by broad line wings. These broad wings can be affected by residuals in the continuum as well as nearby lines, such as CRRL  $\beta$  ( $\Delta n = 2$ ),  $\gamma$  ( $\Delta n = 3$ ) and  $\delta$  ( $\Delta n = 4$ ) lines. In order to obtain the best possible fit, we performed a different stacking procedure to optimize the continuum baseline in the LBA line spectra. This procedure is described in detail in Salas et al. (in preparation) and is similar to the procedure used by Stepkin et al. (2007) for their low-frequency CRRL spectra.

Here, we shortly summarize the main aspects of this procedure. For each stack, the spectra are first searched for CRRL  $\alpha$  and  $\beta$  lines which are unblended with other lines and unaffected by RFI and bandpass roll-off. These lines are then stacked and fitted with Voigt profiles to create template line profiles. These profiles are subtracted from each (unstacked) line spectrum, and the residual spectra are stacked to search and fit for the CRRL  $\gamma$  lines. These  $\gamma$  lines are then also subtracted from the individual line spectra, and one final stack is performed to search and fit for the  $\delta$  lines and also remove those from the individual line spectra. The residual baseline in the individual line spectra, where all  $\alpha$ ,  $\beta$ ,  $\gamma$  and  $\delta$  lines have been removed, is then baseline corrected by a polynomial of order 0. Using the baseline-corrected spectra, we repeated the stack of the lines.



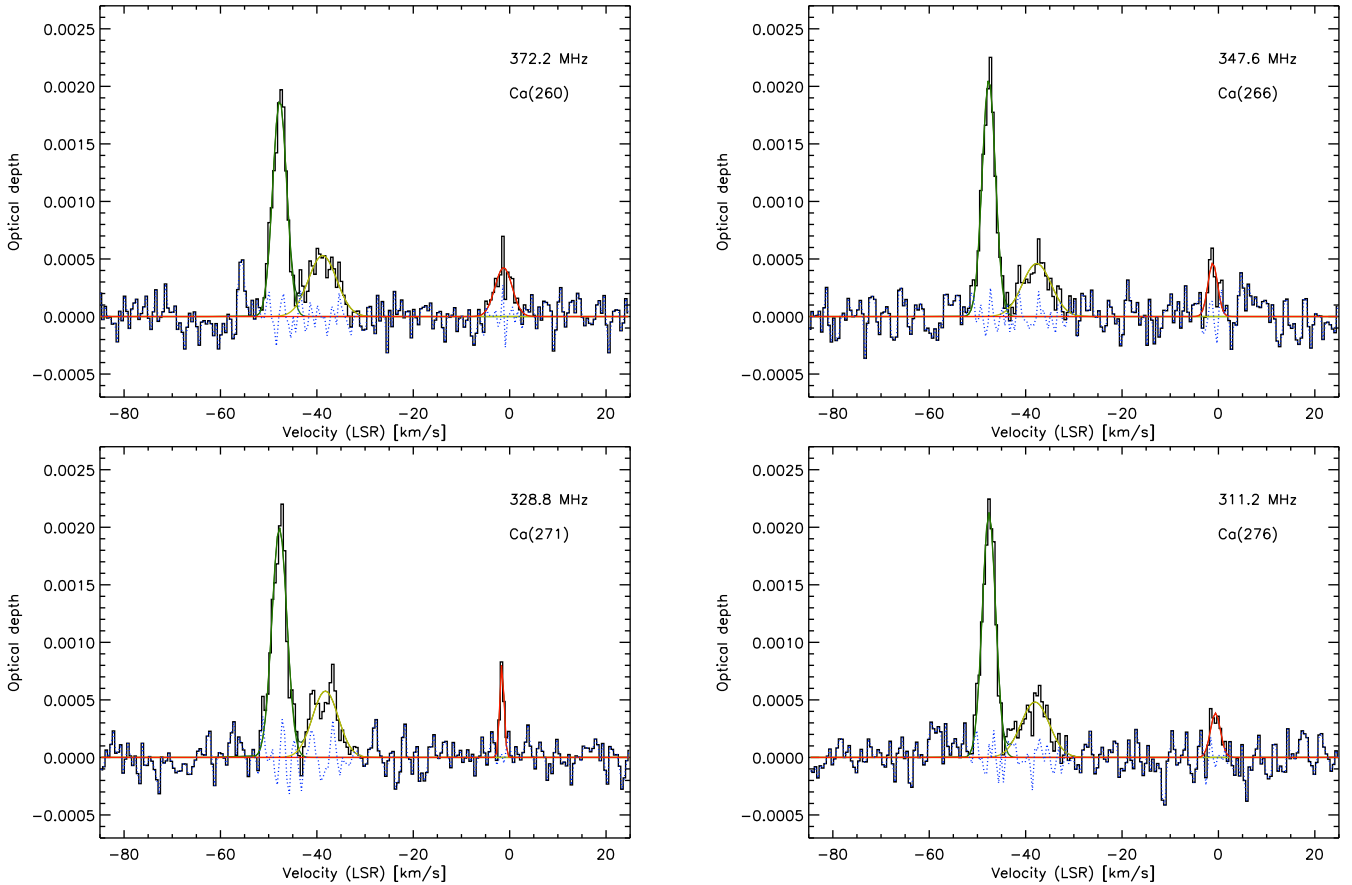


**Figure 2.** WSRT *P*-band 310–390 MHz: stacked CRRL spectra. The green, yellow and red lines show the decomposition into the  $-47$ ,  $-38$  and  $0 \text{ km s}^{-1}$  components. The blue dotted line shows the residuals after subtracting the fitted line profiles.

**Table 3.** WSRT *P*-band measured line properties for  $\text{Cn}\alpha$  recombination line stacks.  $\int \tau dv$  is the integrated optical depth,  $v_{\text{LSR}}$  is the velocity relative to the local standard of rest and  $\text{FWHM}_T$  is total full width at half-maximum. The values are obtained from a Gaussian fit to the spectrum.

Transition ( $n$ )	Frequency (MHz)	$\int \tau dv$ (Hz)	$v_{\text{LSR}}$ ( $\text{km s}^{-1}$ )	$\text{FWHM}_T$ ( $\text{km s}^{-1}$ )
260	372.2	$-8.54 \pm 0.29$	$-47.71 \pm 0.06$	$3.43 \pm 0.13$
		$-4.85 \pm 0.41$	$-38.81 \pm 0.28$	$6.89 \pm 0.69$
266	347.6	$-8.27 \pm 0.28$	$-47.63 \pm 0.05$	$3.24 \pm 0.13$
		$-4.06 \pm 0.42$	$-37.70 \pm 0.36$	$7.10 \pm 0.86$
271	328.8	$-8.48 \pm 0.32$	$-47.76 \pm 0.07$	$3.65 \pm 0.16$
		$-4.23 \pm 0.41$	$-38.24 \pm 0.30$	$6.32 \pm 0.72$
276	311.2	$-7.60 \pm 0.24$	$-47.60 \pm 0.05$	$3.24 \pm 0.12$
		$-3.68 \pm 0.34$	$-38.05 \pm 0.31$	$6.93 \pm 0.76$

This procedure is repeated five times on the LBA spectra by increasing the polynomial order by one in each step. Finally, stacked spectra with only one kind of transition are obtained by removing the corresponding best-fitting Voigt profiles from the individual spectra. The  $\alpha$  line spectra resulting from this procedure are shown in Figs 4 and 5. The baseline-corrected, stacked line spectra are then fitted with Voigt profiles for each of the three velocity components. The results are summarized in Table 5. The line broadening continues to increase towards lower frequencies, and below 40 MHz ( $n = 550$ ), it is no longer possible to robustly disentangle the  $-47$  and  $-38 \text{ km s}^{-1}$  components.

In Salas et al. (in preparation), we have verified this baseline-correction procedure with detailed simulated LOFAR spectra which have the same resolution and noise characteristics as our observations and are processed in the same manner. In the LBA range studied here, this baseline-correction procedure provides only a minor improvement in our recovery of the line profiles. However, this procedure becomes increasingly important at frequencies below 33 MHz. This spectral line stacking procedure with baseline-correction processing, as described above, is used only for the CRRL stacks as it removes all unidentified line features. Upper limits to the undetected recombination lines from hydrogen (HRRLs; Table 6) are obtained from stacked spectra without these corrections applied. In this paper, we will discuss only the  $\alpha$  lines for carbon and hydrogen. The  $\beta$ ,  $\gamma$  and  $\delta$  lines will be discussed in a future paper.

### 3 RESULTS

The WSRT spectra clearly show that there are at least three CRRL velocity components in emission at  $-47$ ,  $-38$  and  $0 \text{ km s}^{-1}$  relative to the local standard of rest (LSR; see Figs 2 and 3). This is consistent with previous measurements by, e.g. Payne et al. (1989, hereafter PAE89) and Kantharia et al. (1998a, hereafter KAP98). In addition, the WSRT spectra also show evidence for the presence of a weak line near  $-55 \text{ km s}^{-1}$ . It is the most prominent at the highest frequency stack, but observed at the  $3\sigma$  level in all stacks (e.g. Fig. 2). A similar feature is not seen in  $\text{H I}$  absorption or CO emission

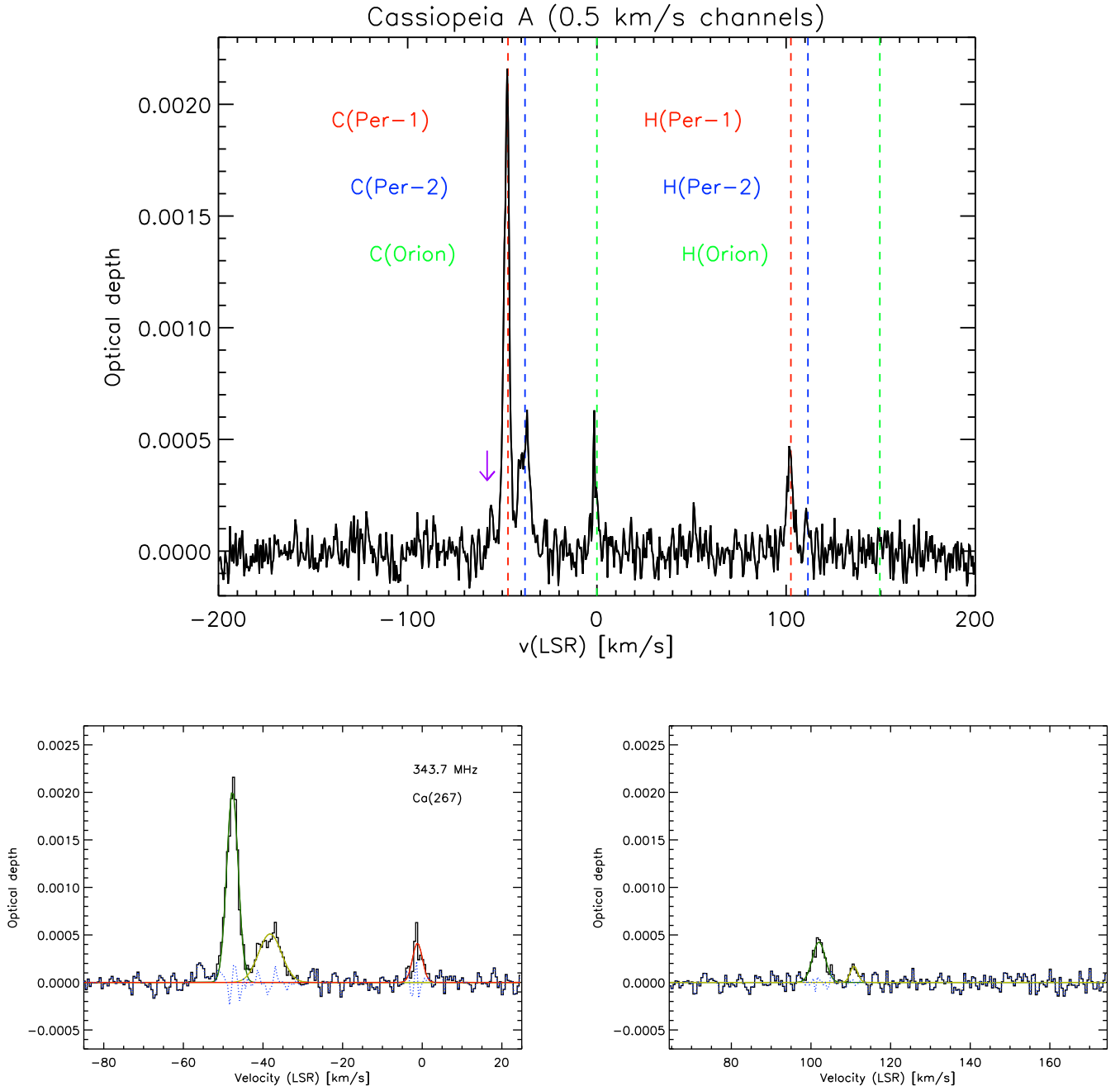


**Figure 3.** WSRT *P*-band stacked, over the full band, RRL spectra. The spectra are centred for CRRLs on  $v(\text{LSR}) = 0.0 \text{ km s}^{-1}$  and spatially integrated over the remnant. Gaussian fits to the RRL lines are shown by the green ( $-47$  component), yellow ( $-38$  component) and red ( $0$  component) solid lines in the bottom spectra. Top panel: stacked WSRT RRL spectrum showing both the CRRLs and HRRLs. The purple arrow shows the location of the SRRL feature at  $-55 \text{ km s}^{-1}$ . Bottom left-hand panel: zoom in on the CRRL components. Bottom right-hand panel: zoom in on the HRRL components. In the bottom panels, the green, yellow and red lines show the decomposition into the  $-47$ ,  $-38$  and  $0 \text{ km s}^{-1}$  components, and the blue dotted line shows the residuals after subtracting the fitted line profiles.

spectra (e.g. Bieging et al. 1991; Mookerjee et al. 2006; Kilpatrick et al. 2014), which makes it unlikely that it is associated with CRRL from another cold cloud at this velocity. A more likely explanation is that this feature is associated with RRL emission from sulphur (SRRL) and/or other elements at higher atomic numbers (sometimes referred to as XRRL or ZRRL) from the  $-47 \text{ km s}^{-1}$  cloud.

Here, we will focus on the CRRL and HRRL emission from the  $-47$  and  $-38 \text{ km s}^{-1}$  velocity components which arise in clouds situated in the Perseus arm. The  $-38$  feature is rather broad, and

the WSRT spectra show tentative evidence that this feature may in fact consist of more than one component. This can also be seen in the asymmetric line profiles of CO emission (Liszt & Lucas 1999; Mookerjee et al. 2006; Kilpatrick et al. 2014) and  $\text{H I}$  21-cm absorption (Bieging et al. 1991; Schwarz et al. 1997). In particular, the CO ( $J = 2-1$ ) emission spectrum from Liszt & Lucas (1999) and Mookerjee et al. (2006) shows two emission peaks, one at  $-40$  and the other at  $-36 \text{ km s}^{-1}$ . For our current analysis, we will treat the  $-38$  feature as a single component.

**Table 4.** WSRT stacked, over the full band, CRRL, HRRL and SRRL  $\alpha$  line profile properties for the line of sight to Cas A. The average frequency is 343.7 MHz, which corresponds to  $n = 267$ .  $v_{\text{LSR}}$  is the velocity relative to the local standard of rest,  $\text{FWHM}_T$  is total full width at half-maximum and  $\int \tau dv$  is the integrated optical depth. The values are obtained from a Gaussian fit to the spectrum. The peak optical depth  $\tau_{\text{peak}}$  is determined directly from the stacked spectrum that has  $0.5 \text{ km s}^{-1}$  channels (see Fig. 3). The  $1\sigma$  spectral rms per  $0.5 \text{ km s}^{-1}$  channel is  $0.5 \times 10^{-4}$  in units of optical depth.

RRL	$v_{\text{LSR}}$ ( $\text{km s}^{-1}$ )	$\text{FWHM}_T$ ( $\text{km s}^{-1}$ )	$\int \tau dv$ (Hz)	$\tau_{\text{peak}}$
S	$-55.70 \pm 0.30$	$2.40 \pm 0.70$	$-0.57 \pm 0.13$	$(2.1 \pm 0.5) \times 10^{-4}$
C	$-47.67 \pm 0.03$	$3.39 \pm 0.08$	$-8.26 \pm 0.16$	$(21.5 \pm 0.5) \times 10^{-4}$
H	$101.99 \pm 0.14$	$3.81 \pm 0.34$	$-1.96 \pm 0.15$	$(4.5 \pm 0.5) \times 10^{-4}$
C	$-38.24 \pm 0.18$	$6.78 \pm 0.44$	$-4.19 \pm 0.23$	$(5.4 \pm 0.5) \times 10^{-4}$
H	$110.80 \pm 0.27$	$2.20 \pm 0.63$	$-0.46 \pm 0.11$	$(1.8 \pm 0.5) \times 10^{-4}$

The WSRT data also show the presence of hydrogen RRLs (HRRLs). These lines are shifted by  $+149.4 \text{ km s}^{-1}$  in the stacked CRRL spectrum (Fig. 3). This difference corresponds exactly to the difference in rest frequencies between the CRRL and HRRL lines. This is only the second detection of HRRLs along this line of sight, and our detection is at a lower frequency than the first detection at 420 MHz by Sorochenko & Smirnov (2010, hereafter SS10). This is the first interferometric detection and the first time that also the weaker  $-38 \text{ km s}^{-1}$  component is detected. For the even weaker Orion spur CRRL component, we did not detect the corresponding HRRLs. If the hydrogen-to-carbon RRL ratio in the Orion spur is similar to that in the Perseus arm components, then this non-detection reflects that even higher signal-to-noise ratio measurements are necessary to detect the HRRLs for the Orion component.

The HRRL for the  $-47 \text{ km s}^{-1}$  component has the same width as the corresponding CRRL, indicating that they both arise in the same gas. However, we notice that the HRRL for the  $-38 \text{ km s}^{-1}$  component has a significantly narrower width than the corresponding CRRL. This may constitute additional evidence that the  $-38 \text{ km s}^{-1}$  CRRL component consists of multiple velocity components and that the HRRLs trace only part of this.

The observed CRRL LBA spectra also show three CRRL velocity components, but they appear in absorption (see Figs 4 and 5). The relative LBA line centroids at  $-47$ ,  $-38$  and  $0 \text{ km s}^{-1}$  (relative to LSR) are consistent with the CRRL emission from WSRT; however, the linewidths in the LBA range are observed to strongly increase in width with decreasing frequency (i.e. increasing  $n$ ). This is expected, and in Section 4.1, we will model this with collisional and radiation broadening. For  $n > 550$ , the increase in linewidth of the  $-47$  and  $-38$  components becomes so large that deblending these components becomes degenerate, and as such, we will consider only the  $n < 550$  measurements in our analysis. The good correspondence between the absorption in the LBA and the emission in WSRT (Fig. 6) indicates that all of the CRRL-emitting gas is situated in front of CasA. HRRLs were not detected in the LBA spectra, and  $3\sigma$  upper limits are presented in Table 6.

#### 4 RRL MODELLING

The CRRL  $\alpha$  ( $\Delta n = 1$ ) transition spectra for both WSRT and the LBA allow us to distinguish at least three velocity components at  $-47$ ,  $-38$  and  $0 \text{ km s}^{-1}$ . The measurements for the  $0 \text{ km s}^{-1}$  component, associated with the Orion spur, will be treated in a

forthcoming paper. Here, we will focus on interpreting the CRRL  $\alpha$  transitions ( $\Delta n = 1$ ) emission from the  $-47$  and  $-38 \text{ km s}^{-1}$  components, which are known to arise from clouds in the Perseus spiral arm (e.g. PAE89). We will use the high signal-to-noise ratio stacked line spectra for our analysis (Figs 2, 4 and 5). These CRRL spectra provide us with two observables to be modelled: (i) the linewidth, and (ii) the optical depth. Both depend on the physical conditions of the emitting gas. In the following, we will first model the linewidth and then the optical depth. We will use the new CRRL models from Salgado (2016a,b, hereafter S16a and S16b, respectively). We find that combining the constraints from both observables is useful to disentangle the degeneracy between electron temperature, electron density and radiation field (see Section 4.3).

We adopt a homogeneous slab with constant density ( $n_e$ ), temperature ( $T_e$ ) and size ( $L_{\text{CII}}$ ). Equivalently, we could have selected the emission measure instead of the size of the cloud. This slab is bathed in an isotropic radiation field characterized by  $T_R \propto \lambda^\beta$  with  $\beta = 2.6$  and normalized in terms of  $T_{R,100}$ , the value of  $T_R$  at 100 MHz. The level populations are fully described by the atomic physics involved (S16a; S16b). Following Seaton (1959) and Brocklehurst (1970), we define the departure coefficient  $b_n$  of level  $n$  as the weighted sum of the  $b_{nl}$  values (S16a). Here  $b_{nl} = N_{nl}/N_{nl}(\text{LTE})$ , with  $N_{nl}(\text{LTE})$  the level populations as given by the Saha–Boltzmann equation under local thermal equilibrium (LTE) conditions. We also introduce  $\beta_n$  as the correction factor for stimulated emission following Brocklehurst & Seaton (1972) and S16a. The  $b_n$  and  $\beta_n$  fully determine the optical depth given by a set of physical conditions  $T_e$ ,  $n_e$  and  $T_R$ . In principle, the intensity also depends on the temperature of the background source, but, in our analysis, we will assume that the intensity scales directly with the optical depth. S16b have shown that this is in general the case for quantum levels above 200, and we verify this a posteriori in Section 4.3. In our analysis, we use the models developed by S16a and S16b, which solve the statistical equilibrium equations for arbitrary  $n$  and  $\ell$  levels in terms of  $b_n$  and  $\beta_n$  as a function  $T_e$ ,  $n_e$  and  $T_R$  fully self-consistently. The gas density and temperature, together with the radiation temperature, also set the radiation and pressure line broadening at high  $n$  (S16a and S16b). We assume a filling factor of 1 for the CRRL-emitting gas and address this point further in Section 4.4.

Previous studies of CRRLs have been analysed following the models by Walmsley & Watson (1982) and Ponomarev & Sorochenko (1992). Because of the limited computer power available at that time, considerable approximations had to be made, and these models are not appropriate for quantitative analysis (S16a). In particular, as compared to previous models, we note that the  $b_n$  values for the models by S16a approach 1 faster at high  $n$ , i.e.  $n \gtrsim 500$ – $600$ , and as such, the corresponding  $b_n \times \beta_n$  values are smaller and have a significantly flatter behaviour at these high  $n$ .

We have used the models by S16a to create a detailed ( $T_e$ ,  $n_e$ ,  $T_R$ ) model grid for fitting our measurements. This grid is sampled in steps of 5 K for  $T_e$  in the range of 10–150 K and in steps of  $0.005 \text{ cm}^{-3}$  for  $n_e$  in the range of  $0.01$ – $0.11 \text{ cm}^{-3}$ . In addition, this grid is computed with a non-zero Galactic power-law radiation field  $T_R$  which is as specified above. For all  $T_e$  and  $n_e$  combinations in our grid, we computed the departure coefficients for five values of  $T_{R,100}$ : 800, 1200, 1400, 1600 and 2000 K. This range in  $T_{R,100}$  covers the range in expected values for the radio continuum temperature from the Milky Way along the line of sight to Cas A (e.g. Landecker & Wielebinski 1970; Haslam et al. 1982; Roger et al. 1999). We will fit our data using a chi-squared method on this grid while adjusting the size of the cloud.

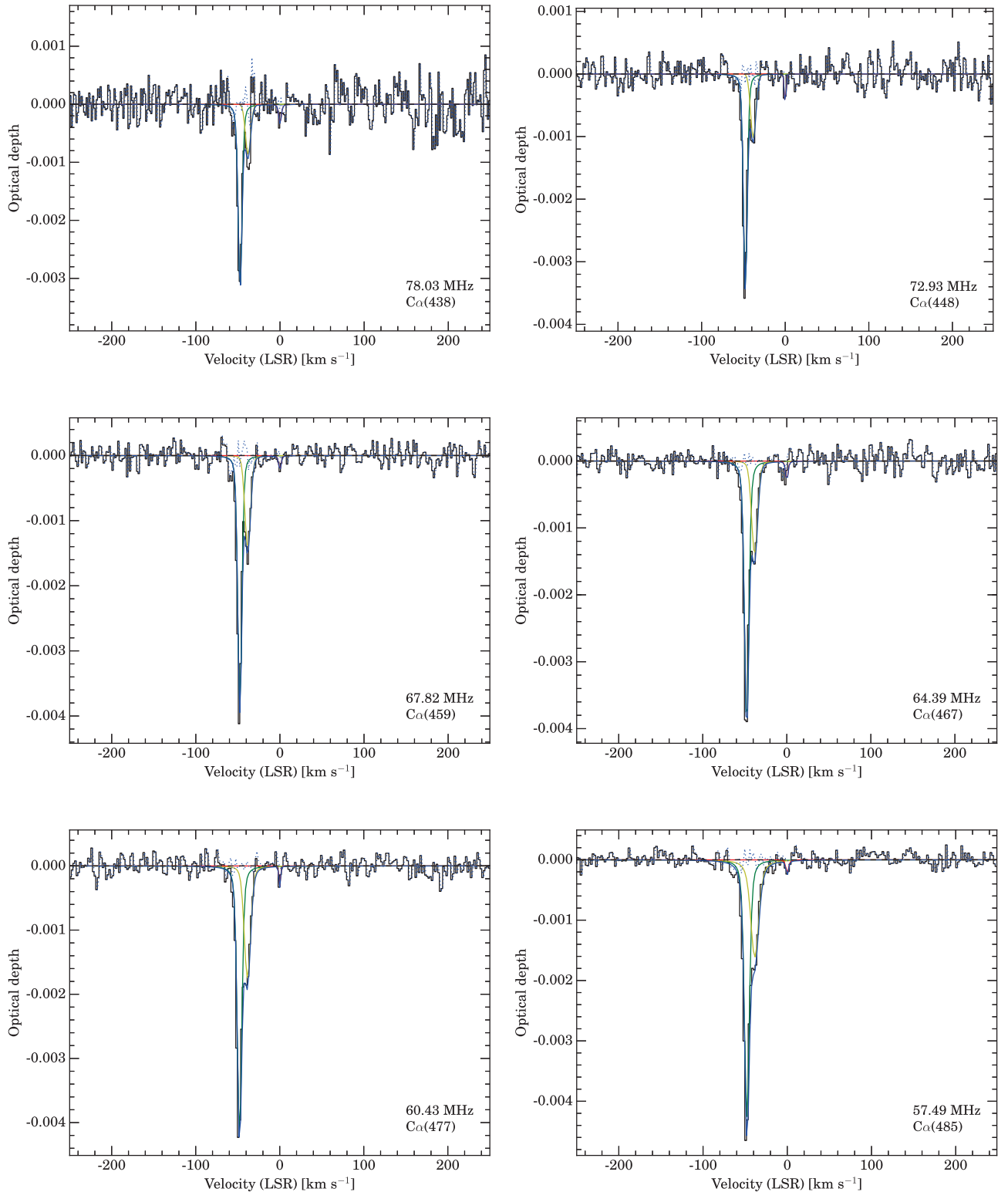


**Figure 4.** LOFAR LBA 55–78 MHz: stacked CRRL spectra. The green, yellow and red lines show the decomposition into the  $-47$ ,  $-38$  and  $0 \text{ km s}^{-1}$  components. The blue dotted line shows the residuals after subtracting the fitted line profiles.

#### 4.1 Linewidth

The measured FWHM linewidth for CRRLs depends on the instrumental resolution and three physical broadening terms: (i) Doppler, (ii) collisional, and (iii) radiation broadening (Shaver 1975; S16b).

The Doppler term is independent of frequency and set by the turbulence of the gas. The Doppler broadening is determined from the WSRT data and literature data at higher frequencies. We find that our WSRT data in the 300–390 MHz range are consistent with the previously measured linewidth at 560 MHz by KAP98 and show



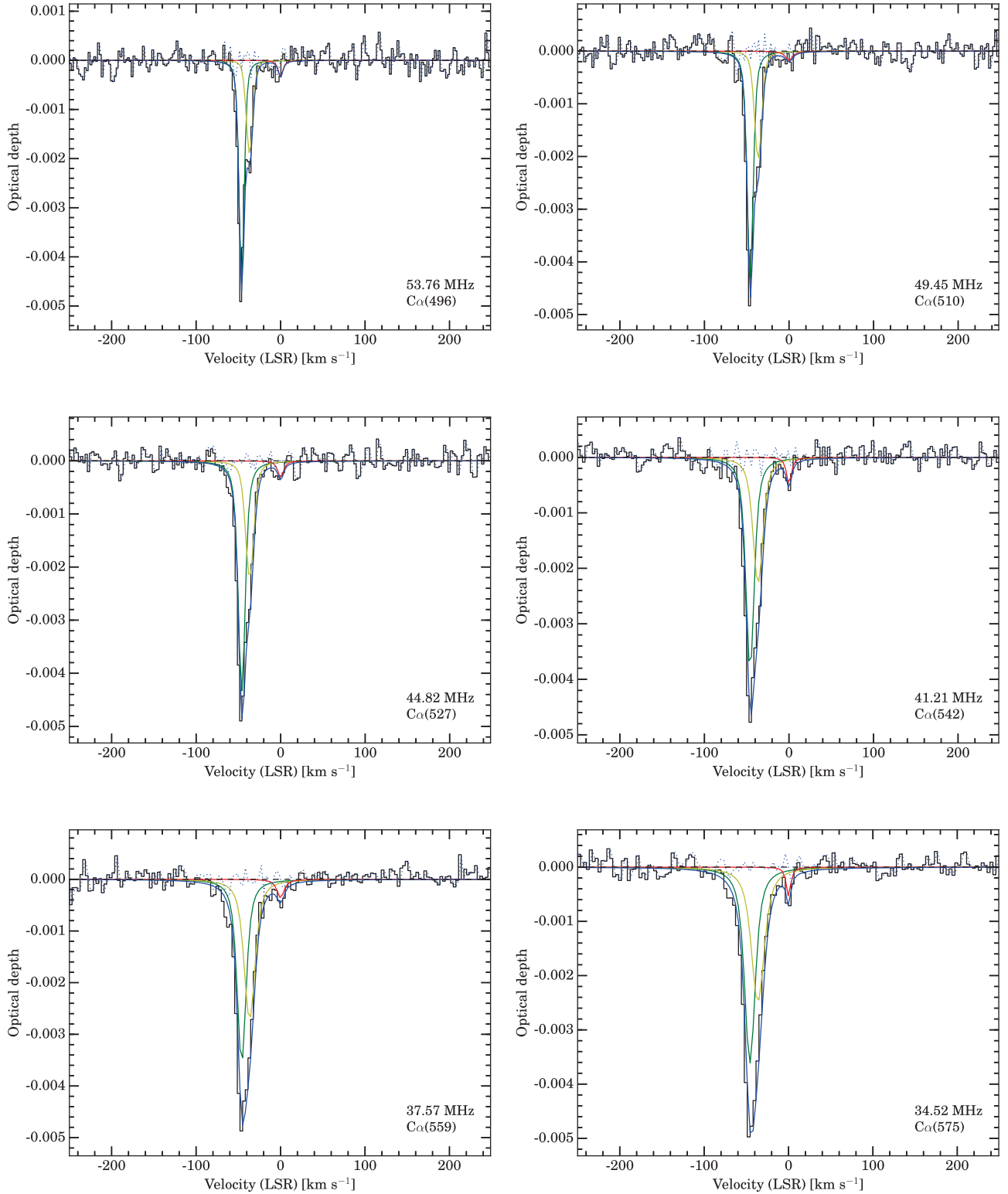


**Figure 5.** LOFAR LBA 56–33 MHz: stacked CRRL spectra. The green, yellow and red lines show the decomposition into the  $-47$ ,  $-38$  and  $0 \text{ km s}^{-1}$  components. The blue dotted line shows the residuals after subtracting the fitted line profiles.

no evidence for line broadening. From this, we conclude that the linewidth in this range is dominated by Doppler broadening and derive a Doppler linewidth of  $3.4 \text{ km s}^{-1}$  for the  $-47 \text{ km s}^{-1}$  component and  $6.8 \text{ km s}^{-1}$  for the  $-38 \text{ km s}^{-1}$  component (Tables 3 and 4).

Whereas the WSRT data show constant linewidths, dominated by Doppler broadening, the LBA data show a clear increase in the FWHM with increasing  $n$ , as expected from pressure and radiation broadening. Having determined the Doppler contribution, which is modelled as a Gaussian, to the line profile, we proceed to

**Table 5.** LOFAR LBA: measured line properties for Cn $\alpha$  recombination line stacks. In our line profile fitting procedure, we have fixed the velocity offset between the  $-47$  and the  $-38$  km s $^{-1}$  components to 9.4 km s $^{-1}$ . For  $n > 550$ , the line blending of the two Perseus arm components is so severe that fitting two components, although necessary to describe the total line profile, is very sensitive to the local spectral noise and bandpass features. We therefore do not use decomposed optical depth and linewidth values for the individual components above  $n = 500$ . Note that there is a small constant offset in velocity of 1–2 km s $^{-1}$  between the second LBA ( $n = 438$ –485) and the first LBA ( $n = 496$ –575) observations. This is due to the inaccuracies in our offline Doppler correction. We have not attempted to correct this as it does not influence the results for the integrated optical depth or the linewidth. FWHM $_T$  is the total full width at half-maximum and FWHM $_L$  is the Lorentzian contribution.

Transition ( $n$ )	Frequency (MHz)	$\int \tau dv$ (Hz)	$v_{LSR}$ (km s $^{-1}$ )	FWHM $_T$ (km s $^{-1}$ )	FWHM $_L$ (km s $^{-1}$ )	Observation
438	78.03	$5.63 \pm 0.50$	$-47.39 \pm 1.46$	$5.60 \pm 0.55$	–	2
		$1.75 \pm 0.50$	[ $-37.99$ ]	$7.41 \pm 0.54$	–	2
448	72.93	$5.58 \pm 0.27$	$-47.69 \pm 1.57$	$5.56 \pm 0.57$	$1.64 \pm 0.30$	2
		$1.97 \pm 0.21$	[ $-38.29$ ]	$7.49 \pm 0.54$	–	2
459	67.82	$6.15 \pm 0.26$	$-47.66 \pm 1.69$	$5.80 \pm 0.57$	$1.75 \pm 0.26$	2
		$2.89 \pm 0.30$	[ $-38.26$ ]	$8.10 \pm 0.56$	$0.92 \pm 0.94$	2
467	64.39	$6.61 \pm 0.24$	$-47.69 \pm 1.78$	$6.27 \pm 0.57$	$2.31 \pm 0.23$	2
		$2.96 \pm 0.28$	[ $-38.29$ ]	$8.61 \pm 0.58$	$1.68 \pm 0.88$	2
477	60.43	$6.81 \pm 0.21$	$-47.86 \pm 1.89$	$6.50 \pm 0.57$	$2.42 \pm 0.20$	2
		$3.79 \pm 0.25$	[ $-38.46$ ]	$9.11 \pm 0.58$	$2.35 \pm 0.65$	2
485	57.49	$7.30 \pm 0.25$	$-47.95 \pm 1.99$	$6.99 \pm 0.57$	$2.95 \pm 0.23$	2
		$(4.71 \pm 0.34)$	[ $-38.55$ ]	$(11.61 \pm 0.67)$	$(6.06 \pm 0.87)$	2
496	53.76	$7.47 \pm 0.47$	$-46.10 \pm 2.13$	$7.29 \pm 0.60$	$3.10 \pm 0.45$	1
		$3.82 \pm 0.54$	[ $-36.70$ ]	$9.47 \pm 0.63$	$2.54 \pm 1.33$	1
510	49.45	$7.97 \pm 0.54$	$-45.89 \pm 2.31$	$8.48 \pm 0.63$	$4.44 \pm 0.54$	1
		$4.41 \pm 0.61$	[ $-36.49$ ]	$10.57 \pm 0.67$	$3.99 \pm 1.30$	1
527	44.82	$8.82 \pm 0.60$	$-46.02 \pm 2.55$	$10.01 \pm 0.66$	$6.09 \pm 0.58$	1
		$5.13 \pm 0.63$	[ $-36.62$ ]	$12.01 \pm 0.69$	$5.79 \pm 1.11$	1
542	41.21	$8.74 \pm 0.91$	$-45.95 \pm 2.78$	$11.92 \pm 0.75$	$8.19 \pm 0.90$	1
		$6.16 \pm 0.90$	[ $-36.55$ ]	$14.52 \pm 0.78$	$8.97 \pm 1.21$	1
559	37.57	$(7.95 \pm 1.00)$	$(-46.03 \pm 3.04)$	$(12.76 \pm 0.77)$	$(8.75 \pm 0.99)$	1
		$(7.43 \pm 1.00)$	[ $-36.63$ ]	$(15.82 \pm 0.75)$	$(10.30 \pm 0.99)$	1
575	34.52	$(9.05 \pm 1.34)$	$(-45.76 \pm 3.31)$	$(15.17 \pm 0.87)$	$(11.31 \pm 1.22)$	1
		$(7.61 \pm 1.29)$	[ $-36.36$ ]	$(18.67 \pm 0.82)$	$(13.58 \pm 1.11)$	1

**Table 6.** Integrated optical depth limits ( $3\sigma$ ) for the non-detected Hn $\alpha$  lines for hydrogen (HRRL) in the LOFAR LBA range. For the HRRL, we use the stacked LBA spectra without baseline correction processing. The upper limits for the integrated optical depth are calculated from  $\tau_{rms,chn}$  and by assuming that the HRRLs are at the same velocity and have the same width as CRRLs.

Transition ( $n$ )	Frequency (MHz)	$\int \tau dv$ ( $3\sigma$ ) (Hz)	$v_{LSR}$ (km s $^{-1}$ )
439	77.46	0.410	$-47$
		0.472	$-38$
447	73.38	0.212	$-47$
		0.246	$-38$
458	68.23	0.151	$-47$
		0.178	$-38$
466	64.78	0.140	$-47$
		0.163	$-38$
475	61.17	0.136	$-47$
		0.162	$-38$
485	57.46	0.111	$-47$
		0.143	$-38$
496	53.73	0.165	$-47$
		0.189	$-38$
510	49.43	0.163	$-47$
		0.182	$-38$
527	44.80	0.130	$-47$
		0.143	$-38$
542	41.19	0.108	$-47$
		0.119	$-38$
559	37.55	0.087	$-47$
		0.097	$-38$
575	34.50	0.110	$-47$
		0.122	$-38$

analyse the remaining line broadening in terms of pressure and radiation broadening. Both these terms are modelled as Lorentzians, and in order to properly recover the Lorentzian line wings, we use the high signal-to-noise ratio line profiles obtained from our line-stacking procedure (Section 2.3). We find that the linewidths for the highest frequency stack ( $n = 438$ ) in the LBA are still consistent with pure Doppler broadening (see also Fig. 6), after which the Lorentzian contribution is found to increase and dominates the overall line profile for  $n > 540$ . The total Lorentzian contribution to the line profile as a function of  $n$  in the LBA range is presented in Table 5.

Collisional and radiation broadening are manifestations of the Stark effect and depend on the physical conditions of the gas and its environment in terms of the electron temperature  $T_e$ , the electron density  $n_e$  and the ambient radiation field  $T_R$  (Shaver 1975; Brocklehurst & Salem 1977; Walmsley & Watson 1982; Gordon & Sorochenko 2009; S16b). We use the formulation by S16b for both collisional and radiation broadening. Here, we parametrize the radiation field in terms of a Galactic power-law radiation field, as defined in Section 4.

We calculate the total required Lorentzian contribution to the linewidth in terms of  $T_{R,100}$  as a function of  $T_e$  and  $n_e$  in the ranges of  $T_e = 10$ –310 K and  $n_e = 0.005$ –0.5 cm $^{-3}$ . To avoid uncertainties from severe line blending, we use only the data below  $n = 550$ . The allowed parameter space is presented in Fig. 7. Within the allowed region of parameter space, we find that there is no strong preference for a particular set of physical conditions; that is, all allowed combinations provide similarly good (i.e. reduced  $\chi^2 \sim 1$ ) fits to the data. The non-allowed, i.e. blanked, area in Fig. 7 shows the region of parameter space which would

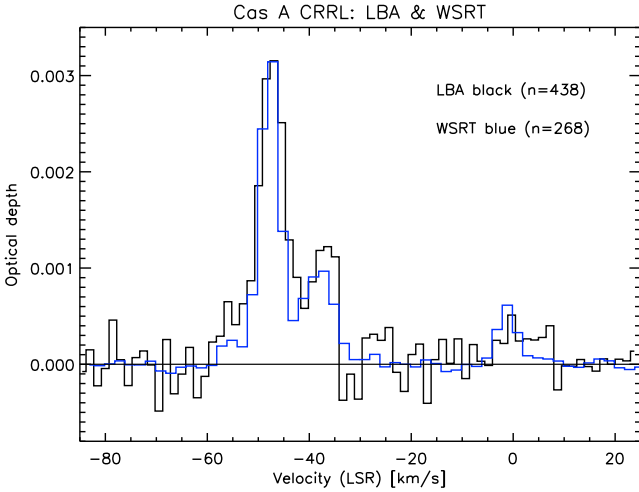


**Figure 6.** Overlay of the WSRT  $P$  band ( $n = 268$ , blue) and LBA ( $n = 438$ , black) stacked CRRL spectra for the line of sight to Cas A. The LBA spectrum has been inverted for this comparison, and the WSRT spectrum was rescaled to match the peak of the  $-47 \text{ km s}^{-1}$  component in the LBA spectrum. The good match of the line profile widths shows that at the highest LBA frequency, the line profile is still dominated by Doppler broadening. Both the WSRT and the (unprocessed bandpass) LBA spectra show an excess at  $-55 \text{ km s}^{-1}$ , which could be associated with sulphur RRLs.

overestimate the observed linewidths beyond the measurement errors.

For both velocity components, constant  $T_{R,100}$  values trace smooth curves in  $(T_e, n_e)$  space, and curves of increasing  $T_{R,100}$  move the allowed set of physical conditions to lower  $T_e$  and  $n_e$  values. Both pressure and radiation broadening have a very similar dependence on quantum number, and hence, fitting the data is degenerate (Shaver 1975; S16b). As both give rise to Lorentzian profiles, their contributions to the line broadening are additive. For any given ra-

diation field, we can then subtract the radiation-broadening component and derive the contribution required from pressure broadening. That will leave us with a relationship between the density and temperature of the gas, which is  $n_e \times T_e^{-0.5}$  (S16b). Figs 7–9 illustrate this for a number of different values for  $T_{R,100}$ . With increasing radiation field temperature, this relationship shifts down. As these figures demonstrate, a large fraction of the parameter space is not allowed.

We see in Section 4.2 that the opposite behaviour is found upon modelling the integrated optical depth, and therefore, the constraints obtained from modelling the linewidth provide us with useful information which is able to break the degeneracy between the different physical parameters. Finally, we note that not only the  $-38 \text{ km s}^{-1}$  component has a broader Doppler contribution than the  $-47 \text{ km s}^{-1}$  component, but also its Lorentzian contribution increases slightly faster with increasing  $n$  than the  $-47 \text{ km s}^{-1}$  component. This may indicate that the physical conditions differ between the  $-47$  and the  $-38$  components, or, alternatively, that the  $-38$  feature consists of multiple velocity components with potentially different physical conditions.

## 4.2 Optical depth

The measured CRRL integrated optical depth depends on  $T_e$ ,  $n_e$ ,  $T_R$  and  $L_{CII}$ , or equivalently, the emission measure  $EM_{CII} = n_e \times n_{CII} \times L_{CII}$  (Dupree 1969, 1971; Shaver 1975; PAE89; S16a). CRRLs at low frequencies arise from quantum levels  $n$  which are not in LTE, and as such, we need to evaluate the departure coefficients  $b_n$  and  $\beta_n$ . These departure coefficients also depend on  $T_e$ ,  $n_e$  and  $T_R$  (e.g. S16a, and references therein). Here, we have used the models by S16a to create a detailed  $(T_e, n_e, T_R)$  model grid for fitting our measurements, as described in Section 4.

In the following, we perform a grid search to find the best  $(T_e, n_e)$  model describing the data, for each  $T_{R,100}$  value, by optimizing the value of  $L_{CII}$ . In Section 3, we showed that the WSRT

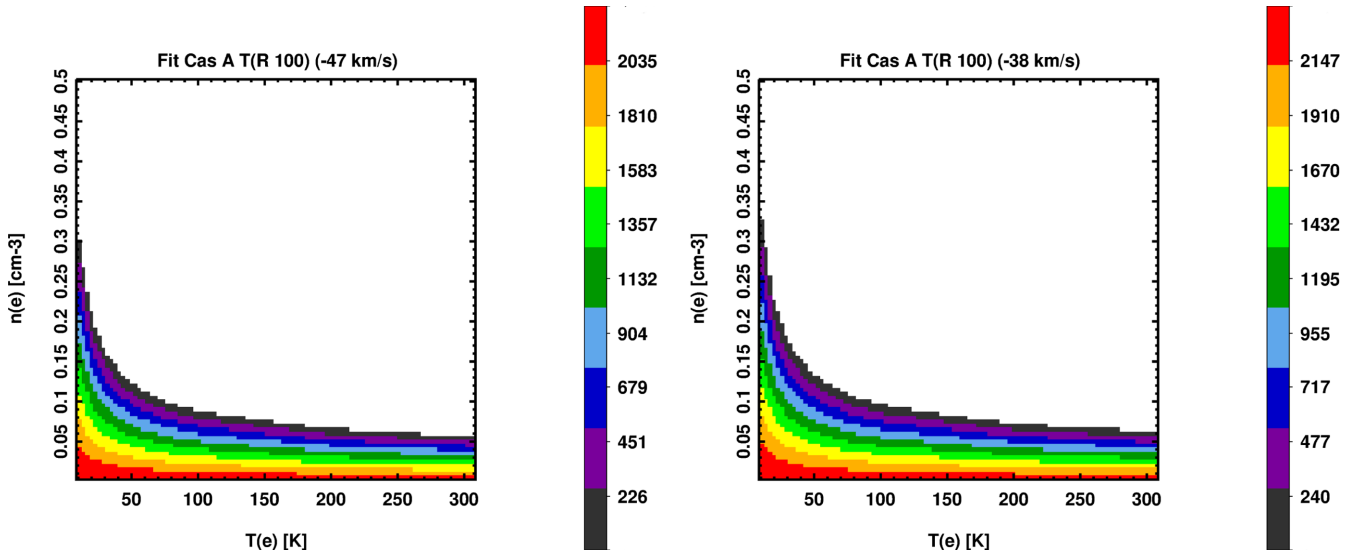


**Figure 7.**  $T_{R,100}$  value as a function of  $T_e$  and  $n_e$  from our model fits to the CRRL linewidth ( $FWHM_L$ ) versus quantum number ( $n$ ) for the Perseus arm components at  $-47 \text{ km s}^{-1}$  (left-hand panel) and  $-38 \text{ km s}^{-1}$  (right-hand panel). For the  $-47 \text{ km s}^{-1}$  component, we find that  $T_{R,100} = 1328 \text{ K}$  for the best-fitting  $(T_e, n_e)$  combination from the optical depths (see also Fig. 10). For the  $-38 \text{ km s}^{-1}$  component, we find that  $T_{R,100} = 1507 \text{ K}$  for the best-fitting  $(T_e, n_e)$  combination from the optical depths (see also Fig. 11). The reduced chi-square values for the points shown for both the  $-47 \text{ km s}^{-1}$  and the  $-38 \text{ km s}^{-1}$  components are all around 1, showing the strong degeneracy between pressure and radiation broadening. The  $1\sigma$  errors associated with  $T_{R,100}$  are independent of  $(T_e, n_e)$  and found to be 83 and 128 K for the  $-47 \text{ km s}^{-1}$  and  $-38 \text{ km s}^{-1}$  components, respectively. Constant  $T_{R,100}$  values trace curves of the form  $n_e \times T_e^{-0.5}$ .

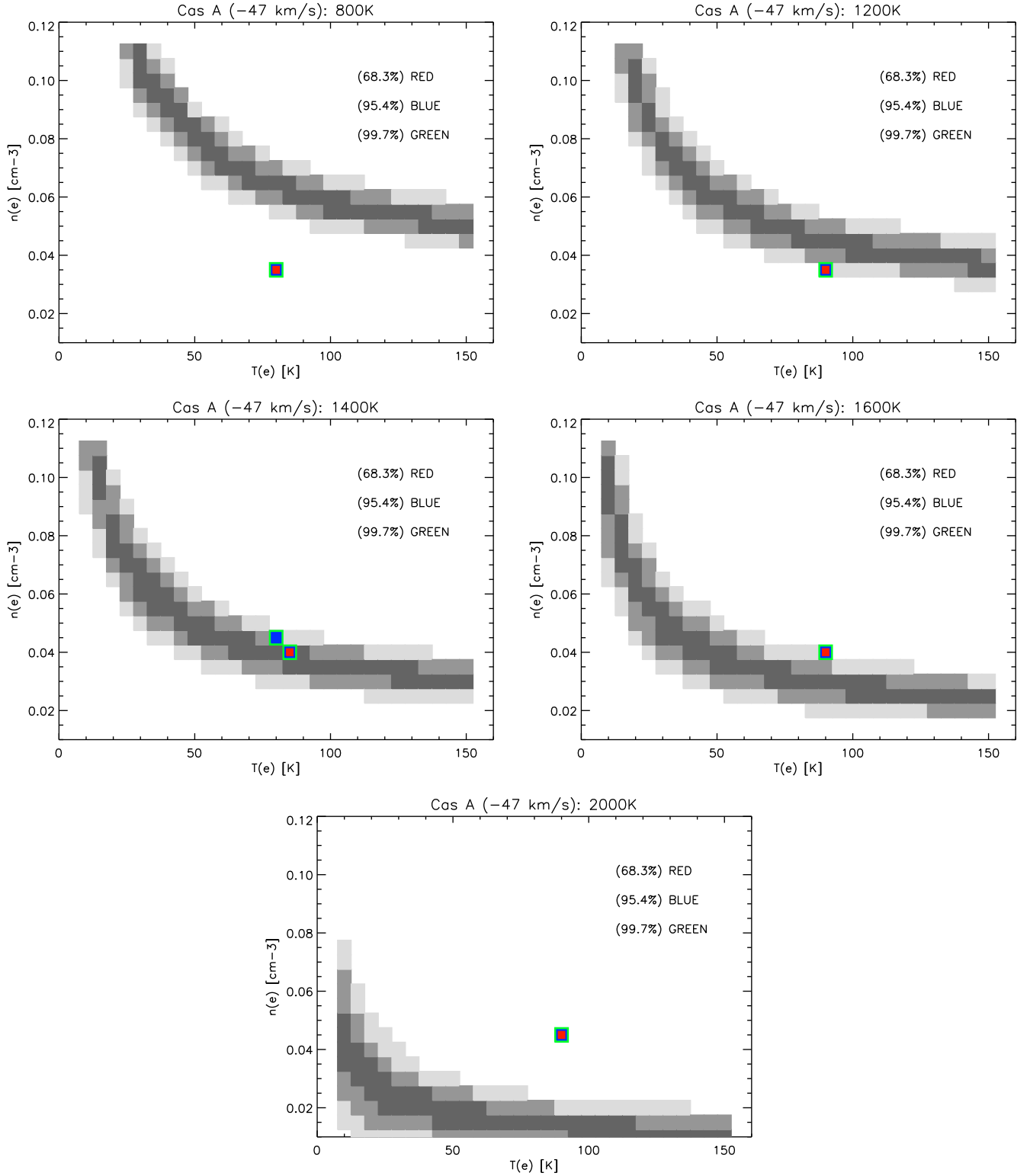


**Figure 8.** Combined model constraints for the CRRL integrated optical depth ( $\tau$ ) and linewidth (FWHM) for the Perseus arm component at  $-47$  km s<sup>-1</sup>. The 1, 2 and 3 $\sigma$  confidence limits from the integrated optical depth fitting are shown by the red, blue and green boxes, respectively. The red and blue boxes should have the same size as the green boxes, but they have been decreased in size for clarity. The 1, 2 and 3 $\sigma$  linewidth error limits are shown by the black, dark-grey and light-grey boxes, respectively. The model fits shown have been carried out for five different  $\text{Tr},100$  values of our  $(T_e, n_e)$  grid: (top left-hand panel)  $\text{Tr},100 = 800$  K; (top right-hand panel)  $\text{Tr},100 = 1200$  K; (middle left-hand panel)  $\text{Tr},100 = 1400$  K; (middle right-hand panel)  $\text{Tr},100 = 1600$  K; and (bottom left-hand panel)  $\text{Tr},100 = 2000$  K.

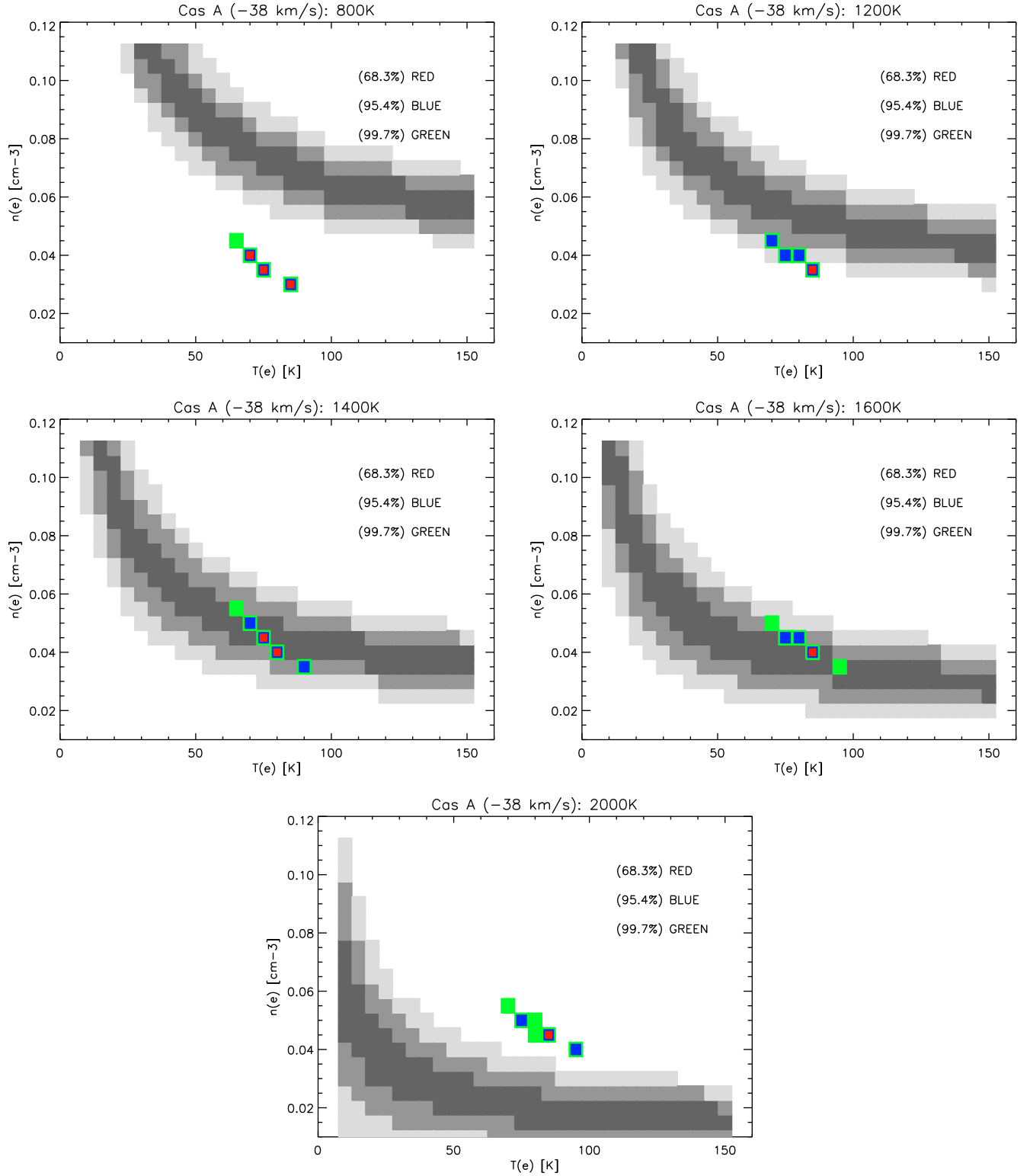


**Figure 9.** Combined model constraints for the CRRL integrated optical depth ( $\tau$ ) and linewidth (FWHM) for the Perseus arm component at  $-38 \text{ km s}^{-1}$ . The 1, 2 and  $3\sigma$  confidence limits from the integrated optical depth fitting are shown by the red, blue and green boxes, respectively. The red and blue boxes should have the same size as the green boxes, but they have been decreased in size for clarity. The 1, 2 and  $3\sigma$  linewidth error limits are shown by the black, dark-grey and light-grey boxes, respectively. The model fits shown have been carried out for five different  $\text{Tr}_{100}$  values of our  $(T_e, n_e)$  grid: (top left-hand panel)  $\text{Tr}_{100} = 800 \text{ K}$ ; (top right-hand panel)  $\text{Tr}_{100} = 1200 \text{ K}$ ; (middle left-hand panel)  $\text{Tr}_{100} = 1400 \text{ K}$ ; (middle right-hand panel)  $\text{Tr}_{100} = 1600 \text{ K}$ ; and (bottom left-hand panel)  $\text{Tr}_{100} = 2000 \text{ K}$ . Our  $(T_e, n_e)$  grid is sampled in steps of  $5 \text{ K}$  for  $T_e$  in the range of  $10\text{--}150 \text{ K}$  and in steps of  $0.005 \text{ cm}^{-3}$  for  $n_e$  in the range of  $0.01\text{--}0.11 \text{ cm}^{-3}$ .



emission and LBA absorption spectra are consistent in terms of the observed absolute and relative velocity centroids of the different CRRL components (see, e.g. Fig. 6). In addition, we found in Section 4.1 that the observed linewidths can be modelled with single physical models across the entire range in  $n$  from 225 to 550. This indicates that it is likely that all of the emitting gas observed from the  $-47$  and  $-38$  km s $^{-1}$  Perseus arm components is situated in front of Cas A and hence can be modelled across the entire range in  $n$  with a single value of  $L_{CII}$  for emission and absorption.

We have selected the  $n = 301$  ( $-47$  km s $^{-1}$  component only) and  $n = 309$  CRRL measurements from PAE89 and the  $n = 225$  CRRL measurement from KAP98 to complement our WSRT and LOFAR measurements upon fitting the models. The other data presented by these authors overlap with our measurements and are consistent with these. We have not added these other measurements as they are either unresolved in velocity or have much lower signal-to-noise ratio as compared to our measurements. In addition, we want to avoid systematic uncertainties by adding measurements obtained with very different observing parameters. Finally, we will consider only measurements with  $n$  in the range of 225–550 as for  $n > 550$ , it is not possible to reliably decompose the  $-38$  and  $-47$  km s $^{-1}$  components. We exclude  $n < 225$  because we calculate the integrated optical depths using equation (6) in S16b. This equation is identical to what has been used in previous studies (e.g. PAE89; KAP98). However, as pointed out by S16b, this equation is not exact, and in the case of a strong background source, the exact radiative transfer equation should be solved; that is, equation (1) in S16b should be used for sufficiently low  $n$  levels. In the case of Cas A, we find that for  $n < 225$  the differences between the approximate and exact solutions start to become significant, i.e. greater than 1 per cent, and hence, we consider only measurements below this  $n$  value (see Section 5.3).

The results of our grid search, in terms of the 1, 2 and  $3\sigma$  confidence limits, are shown by the red, blue and green coloured boxes in Figs 8 and 9 for different values of  $T_{R,100}$ . For the  $-47$  km s $^{-1}$  component, we find no significant difference in the quality (i.e. reduced  $\chi^2 \sim 1$ –2) of the best fit for each of the five different values of  $T_{R,100}$ , but there is a systematic trend in that higher  $T_{R,100}$  values require (slightly) higher values of  $T_e$  and  $n_e$  (see Fig. 8). This trend is the opposite of what we observed for our linewidth modelling in Section 4.1, and we will discuss this in more detail in Section 4.3. Considering the entire parameter space probed by our model grid for the  $-47$  km s $^{-1}$  component, we find that only a very limited region in parameter space is allowed and that we can constrain  $T_e$  to be in the range of 80–90 K and  $n_e$  to be in the range of 0.035–0.045 cm $^{-3}$ . However, the  $T_{R,100}$  value is not well constrained by considering only the integrated optical depth.

For the  $-38$  component, we find similar trends to those for the  $-47$  component in that we obtain equally good fits for each of the five different  $T_{R,100}$  values, and higher  $T_{R,100}$  values require (slightly) higher combinations of  $T_e$  and  $n_e$  to be allowed (see Fig. 9). Given the lower signal-to-noise ratio of the  $-38$  component, the parameter space is slightly larger than for the  $-47$  component. In particular, we see that a larger range in both  $T_e$  and  $n_e$  is allowed. However, this allowed range opens up along a particular curve in  $(T_e, n_e)$  space, which traces an almost constant (electron) pressure  $p_e$ . We will discuss this curve in more detail in Section 5.1. Considering only the integrated optical depth models, we constrain  $T_e$  to be in the range of 70–85 K and  $n_e$  in the range of 0.030–0.045 cm $^{-3}$ . The model fits for the  $-38$  component are not as good as for the  $-47$  component and have a reduced  $\chi^2 \sim 4$ –5. In particular, we note that

**Table 7.** CRRL model results. Here we have adopted the gas phase abundance of carbon by Cardelli et al. (1996) to convert our CRRL measurements into hydrogen column densities  $N_H$ , volume densities  $n_H$  and thermal pressure. The range in magnetic pressures is taken from the measurements by Heiles & Stevens (1986) and Schwarz et al. (1986).

Parameter	Unit	$-47$ km s $^{-1}$	$-38$ km s $^{-1}$
$T_{R,100}$	(K)	1400 (1351 $\pm$ 83)	1600 (1507 $\pm$ 128)
$T_e$	(K)	85 $\pm$ 5	85 $\pm$ 10
$n_e$	(cm $^{-3}$ )	0.040 $\pm$ 0.005	0.040 $\pm$ 0.005
$L_{CII}$	(pc)	35.3 $\pm$ 1.2	18.6 $\pm$ 1.6
$EM_{CII}$	(cm $^{-6}$ pc)	0.056 $\pm$ 0.014	0.030 $\pm$ 0.008
$N_{CII}$	(cm $^{-2}$ )	(4.4 $\pm$ 0.6) $\times 10^{18}$	(2.3 $\pm$ 0.3) $\times 10^{18}$
$N_H$	(cm $^{-2}$ )	(3.1 $\pm$ 0.4) $\times 10^{22}$	(1.6 $\pm$ 0.2) $\times 10^{22}$
$n_H$	(cm $^{-3}$ )	286 $\pm$ 36	286 $\pm$ 36
$p_{thermal}/k$	(K cm $^{-3}$ )	(2.4 $\pm$ 0.5) $\times 10^4$	(2.4 $\pm$ 0.5) $\times 10^4$
$p_{turbulent}/k$	(K cm $^{-3}$ )	(1.9 $\pm$ 0.1) $\times 10^5$	(7.6 $\pm$ 1.0) $\times 10^5$
$p_{magnetic}/k$	(K cm $^{-3}$ )	(1.8–4.5) $\times 10^4$	–
$\zeta_H$	(s $^{-1}$ )	(0.3 $\pm$ 0.05) $\times 10^{-17}$	–

the increase in integrated optical depth in the LBA range is faster with increasing  $n$  than expected from the best-fitting model.

### 4.3 Combining linewidth and optical depth

In Figs 8 and 9, we have shown the independent constraints from both the linewidth and the optical depth in a single plot of  $T_e$  versus  $n_e$  as a function of  $T_{R,100}$ . We note that the constraints from the integrated optical depth are much more stringent than those obtained from the linewidth. However, as stated above, the integrated optical depth does not constrain  $T_{R,100}$  well. The linewidth does not provide very good constraints on either  $T_e$ ,  $n_e$  or  $T_{R,100}$ , but we find that the allowed models for the linewidth move in an opposite direction in  $(T_e, n_e)$  space as compared to the models for the integrated optical depth upon changing  $T_{R,100}$ . Therefore, the combination of the integrated optical depth and linewidth does allow us to constrain  $T_{R,100}$  and thus  $T_e$  and  $n_e$  better.

Considering both measurements, we find that the electron temperature and density for both components can be constrained to better than 15 per cent at the  $1\sigma$  confidence level (see Table 7). We find very similar conditions,  $T_e \sim 85$  K and  $n_e = 0.04$  cm $^{-3}$ , for both components. The background Galactic radiation field is marginally higher for the  $-38$ , as compared to the  $-47$ , component, but both are well within the range measured along the line of sight to Cas A (e.g. Landecker & Wielebinski 1970; Haslam et al. 1982; Roger et al. 1999). The line-of-sight path-length  $L_{CII}$  for these physical conditions is found to be about 35 and 19 pc for the  $-47$  and  $-38$  components, respectively. Here, we have assumed that the singly ionized carbon  $n_{CII}$  density is equal to the free electron density  $n_e$ . The contribution of ionized hydrogen to  $n_e$ , based on the HRRL measurements, is found to be of the order of a few per cent and will be discussed in Section 5.2. This path-length implies C II column densities  $N_{CII}$  of  $4 \times 10^{18}$  and  $2 \times 10^{18}$  cm $^{-2}$  and C II emission measures  $EM_{CII}$  of 0.06 and 0.03 cm $^{-6}$  pc, respectively. The results from the combined linewidth and optical depth constraints are summarized in Table 7 and shown in Figs 10 and 11. The C II emission measure of both components, in terms of the associated free-free absorption, does not violate the observed low-frequency radio continuum turnover of Cas A (e.g. Kassim et al. 1995).

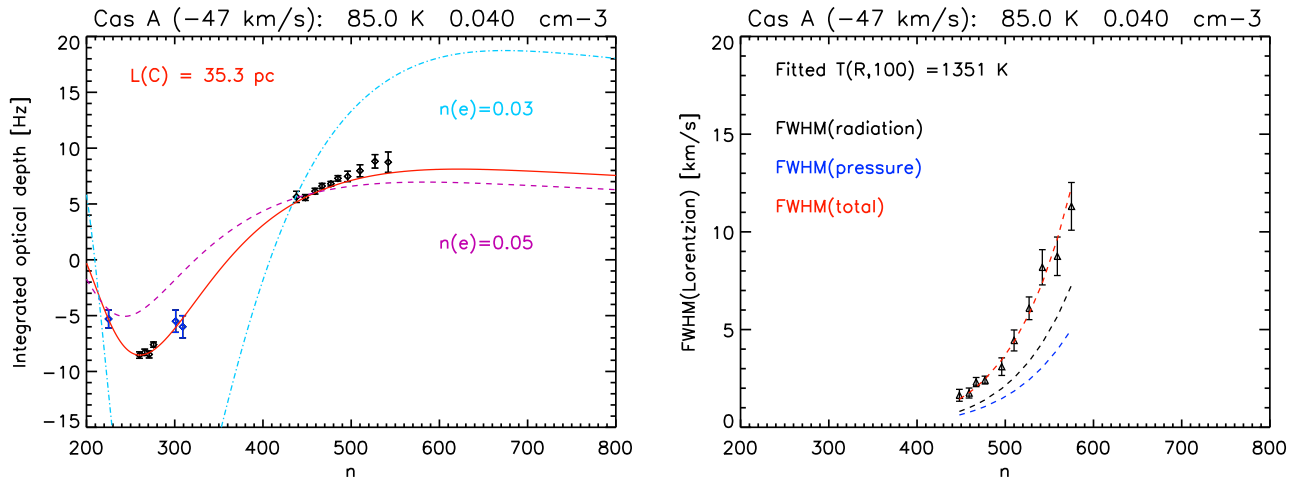


**Figure 10.** Best-fitting CRRL optical depth and linewidth models overlaid on the measurements for the  $-47 \text{ km s}^{-1}$  component. Our LOFAR and WSRT data are shown in black. In addition, we show the literature data which we have used in blue. The literature measurements are taken from Kantharia et al. (1998a) and Payne et al. (1989) for  $n = 225, 301$  and  $309$ . Left-hand panel: The red curve shows the best-fitting optical depth model with  $L_C = 35.3 \text{ pc}$  for  $T_{R,100} = 1400 \text{ K}$ . In addition, we show two optical depth models for the same best-fitting  $T_e$  but with a 25 per cent difference in  $n_e$  (dot-dashed curve:  $n_e = 0.03 \text{ cm}^{-3}$  and dashed curve:  $n_e = 0.05 \text{ cm}^{-3}$ ). Right-hand panel: The red curve shows the best-fitting linewidth model with  $T_{R,100} = 1351 \text{ K}$ . The red curves in both panels have the same  $T_e$  and  $n_e$  values as taken from the best-fitting CRRL optical depth model (see Fig. 8).

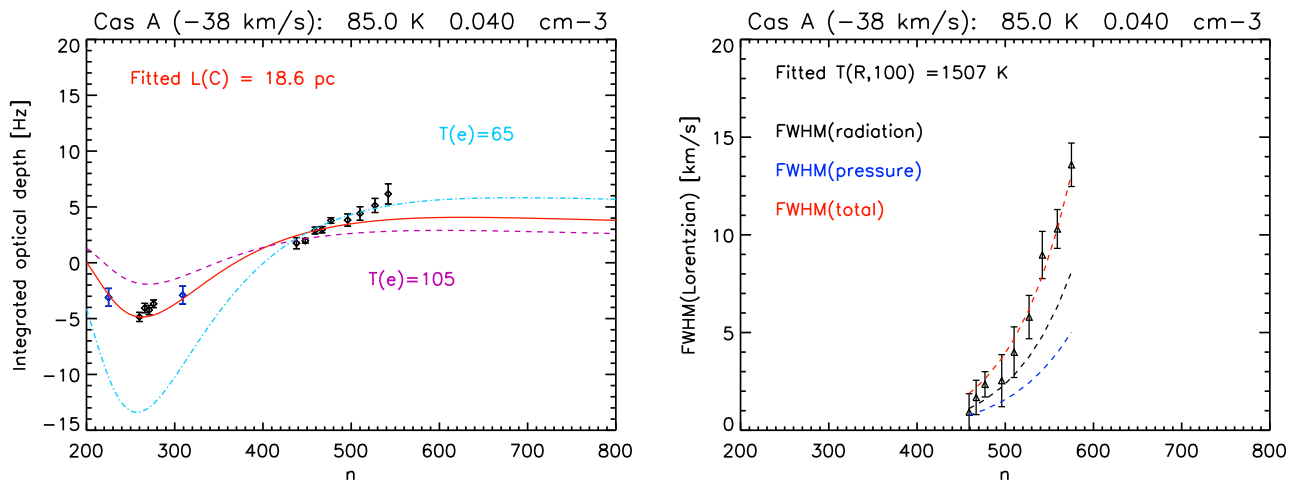


**Figure 11.** Best-fitting CRRL optical depth and linewidth models overlaid on the measurements for the  $-38 \text{ km s}^{-1}$  component. Our LOFAR and WSRT data are shown in black. In addition, we show the literature data which we have used in the fit in blue. The literature measurements are taken from Kantharia et al. (1998a) and Payne et al. (1989) for  $n = 225$  and  $309$ . Left-hand panel: The red curve shows the best-fitting optical depth model with  $L_C = 18.6 \text{ pc}$  for  $T_{R,100} = 1600 \text{ K}$ . In addition, we show two optical depth models for the same best-fitting  $n_e$  but with a 25 per cent difference in  $T_e$  (dot-dashed curve:  $T_e = 65 \text{ K}$  and dashed curve:  $T_e = 105 \text{ K}$ ). Right-hand panel: The red curve shows the best-fitting linewidth model with  $T_{R,100} = 1507 \text{ K}$ . The red curves in both panels have the same  $T_e$  and  $n_e$  values as taken from the best-fitting CRRL optical depth model (see Fig. 9).

#### 4.4 Comparison to earlier studies

PAE89 previously performed a velocity-resolved CRRL investigation of the  $-47$  and  $-38 \text{ km s}^{-1}$  clouds observed along the line of sight to Cas A. As discussed in Section 3, our measurements and those of PAE89 are broadly consistent, albeit that PAE89 have considerably higher scatter and larger errors in their measurements as compared to our data set.

For the linewidth modelling, both PAE89 and we considered a purely Galactic radiation field with a dilution factor of 1. PAE89 considered  $T_{R,100} = 800 \text{ K}$  and Doppler widths of  $6.7$  and  $5.9 \text{ km s}^{-1}$  for the  $-47$  and  $-38 \text{ km s}^{-1}$  components, respectively. The emission-line measurements by PAE89 and this work show that the Doppler width for the  $-47 \text{ km s}^{-1}$  component is overesti-

mated in the modelling by PAE89. Another difference in computing the linewidth between PAE89 and our work is that PAE89 use the Shaver (1975) formulation, whereas we use the updated formulation by S16b. Comparing these we find that S16b predicts lower linewidths for both collisional and radiation broadening for a given combination of  $T_e$ ,  $n_e$  and  $T_R$ . For a Galactic radiation field with  $\beta = 2.6$ , the line FWHM from radiation broadening predicted by S16b is 24 per cent lower and this difference is independent of quantum number  $n$ . The lower values obtained from S16b are due to a more accurate approximation of the oscillator strength by S16b as compared to Shaver (1975). In terms of pressure broadening, the difference is largest at low  $n$  and decreases towards higher  $n$ . This results from a more detailed fitting to the collisional cross-sections in S16b as compared to Shaver (1975). For the physical

conditions of interest here, S16b predicts an FWHM which is about 15 per cent lower at  $n = 200$  and decreases to 5 per cent lower at  $n = 600$ , as compared to Shaver (1975). The total difference in the FWHM thus amounts to about 30 per cent upon considering both broadening terms and, in combination with the different Doppler width, explains the higher Galactic  $T_{R,100}$  values which we obtain here.

PAE89 also performed an investigation of the integrated CRRL optical depths. Our WSRT optical depth measurements for both the  $-47$  and  $-38$  km s $^{-1}$  components at  $n \sim 267$  are about 20 per cent larger than the measurements of PAE89. Given the lower signal-to-noise ratio and narrow bandwidth of the spectra in PAE89, this difference can likely be attributed to uncertainties in the line fitting by PAE89 as well as differences in observing parameters and their calibration. The LBA optical depths at  $n = 438$  to  $448$  are slightly larger than the measurements of PAE89 but consistent within errors. At  $n \sim 500$ , the sum of our measurements for the  $-38$  and  $-47$  components agrees with the sum of the PAE89 measurements; however, the optical depths assigned to each of the two components by PAE89 differ from ours. We find that the lower signal-to-noise ratio and the factor of 2 lower velocity resolution of PAE89 likely makes their deblending more uncertain. At even higher  $n$ , i.e.  $n \sim 575$ , we find that the sum of our  $-38$  and  $-47$  measurements agrees well with the high signal-to-noise ratio measurement at 34 MHz by KAP98.

PAE89 performed a fit to their integrated CRRL optical depth measurements. They, and subsequent work by Payne, Anantharamaiah & Erickson (1994) and KAP98, used the models by Walmsley & Watson (1982) as the basis for their fitting procedures. PAE89 concluded that these models did not provide a satisfactory fit to their data. In particular, they noted that their models could not simultaneously fit both the low- $n$  emission and high- $n$  absorption measurements, and as such, they could not discriminate between cold ( $T_e \sim 20$  K), high-density ( $n_e \sim 0.3$  cm $^{-3}$ ) models and warm ( $T_e \sim 100$  K), lower density ( $n_e \sim 0.05$  cm $^{-3}$ ) models. As described in Section 4, the models by Walmsley & Watson (1982) are not appropriate for a quantitative analysis of the CRRL data.

Most of the previous CRRL optical depth measurements agree well with the new high signal-to-noise ratio measurements presented here. However, a few of the previous measurements are at variance with our data, and, given their lower signal-to-noise ratio, we deem those measurements to be unreliable and exclude them from our analysis. We find that the models by S16a and S16b are able to fit both the CRRL linewidth and the optical depth measurements well over the range  $n = 225$ – $550$  for a single set of physical parameters (Section 4.3 and Table 7).

In our above modelling of the optical depth, we have assumed a filling factor of 1 for the CRRL-emitting gas. Previous studies by PAE89 and KAP98 also assumed this. Given that the H I 21-cm absorption for both the  $-38$  and  $-47$  km s $^{-1}$  components extends over the entire face of the remnant (Bieging et al. 1991; Schwarz et al. 1997) and the good spatial correlation of CRRL with H I 21-cm absorption (Anantharamaiah et al. 1994), we believe that this is a reasonable choice. However, there is spatial structure within the gas on smaller scales, and we will discuss this in more detail in Section 5.3.

## 5 DISCUSSION

Since the study by PAE89, there have been two other detailed investigations of the CRRLs along the Cas A line of sight by Payne et al. (1994) and KAP98. Neither of these studies was able to fit

both the integrated optical depths and the linewidths of the CRRLs for a single set of physical parameters. This is likely due to the reasons outlined in Section 4.4. With the more detailed models by S16a and S16b, we have shown in Section 4.3 that we are now able to obtain a satisfactory fit to both the linewidth and the optical depths.

The derived electron densities of  $\sim 0.04$  cm $^{-3}$  translate into a density of hydrogen nuclei of 286 cm $^{-3}$ , adopting the gas-phase carbon abundance of  $1.4 \times 10^{-4}$  (Cardelli et al. 1996; Sofia et al. 1997). This density is high compared to the typical density of diffuse clouds traced by the 21-cm H I line ( $n_H \sim 50$  cm $^{-3}$ ; Wolfire et al. 2003). However, they are quite comparable to densities derived for the well-studied diffuse sightlines of  $\zeta$  Oph,  $\zeta$  Per and  $\sigma$  Per, where simultaneous modelling of the observations of many atomic and molecular species results in densities in the range of 200–400 cm $^{-3}$  (e.g. van Dishoeck & Black 1986; Viala, Roueff & Abgrall 1988).

The derived temperature of 85 K is well in the range of temperatures derived by the same studies as well as temperatures derived from H I 21-cm-line studies (e.g. Mebold & Hills 1975; Dickey & Benson 1982; Dickey & Lockman 1990; Heiles & Troland 2003). The derived thermal pressure of  $2 \times 10^4$  K cm $^{-3}$  agrees, of course, well with those measured towards  $\zeta$  Oph,  $\zeta$  Per and  $\sigma$  Per, but they are an order of magnitude larger than the typical gas pressures derived from UV absorption lines measuring the C I fine structure line excitation ( $\sim 4 \times 10^3$  K cm $^{-3}$ ; e.g. Jenkins & Tripp 2011).

Finally, our sizes are comparable to the sizes of typical H I diffuse clouds ( $\sim 10$  pc, e.g. Spitzer 1978), but the derived column densities are an order of magnitude higher. These differences may merely reflect that we are probing clouds in the Perseus and Orion spiral arms rather than diffuse clouds in the local Solar neighbourhood. Specifically, the clouds probed by the CRRLs may be the atomic/CO-dark surfaces of molecular clouds. As our clouds are situated in spiral arms and molecular clouds have been detected along the same sightline at the same velocities (Bieging & Crutcher 1986; Liszt & Lucas 1999; Mookerjee et al. 2006; Kilpatrick et al. 2014), this is quite reasonable. We note that it is difficult to keep C II ionized over the large path-lengths inferred here, unless we are viewing the Cas A clouds from a preferred angle. It is therefore likely that the clouds we are observing are sheet-like structures. Filamentary spurs springing off spiral arms are a common characteristic of a turbulent ISM, and these are dominated by atomic and CO-dark molecular gas (Smith et al. 2014).

The inferred pressures are also in line with measured pressures of molecular cloud surfaces (e.g. Blitz & Thaddeus 1980; Heyer, Carpenter & Snell 2001). Moreover, the very similar sightlines towards  $\zeta$  Per and  $\sigma$  Per traverse the atomic H I surfaces associated with the B3/B4/B5 molecular clouds (Andersson, Roger & Wannier 1992). On the other hand, the high H I 21-cm column densities and the implied high visual extinction of these clouds ( $N_{H I} \sim 2 \times 10^{22}$  cm $^{-2}$ ;  $A_V \sim 10$  mag) are very high for atomic clouds ( $N_{H I} \lesssim 2 \times 10^{21}$  cm $^{-2}$ ;  $A_V \lesssim 1$ ; e.g. Dickey & Lockman 1990). Indeed, for visual extinctions in excess of 1 mag, much of the gas-phase carbon is expected to be in CO (and to a lesser extent in C I) rather than C II (e.g. van Dishoeck & Black 1986; Viala et al. 1988). This may just be a matter of geometry as the clouds probed by the CRRL may be arranged into thin sheets as is common for large-scale H I structures (Sancisi et al. 1974; Spitzer & Jenkins 1975; Heiles 1984). Future observations will be instrumental in settling the relationship between the CRRL gas and the molecular clouds in the direction of Cas A.

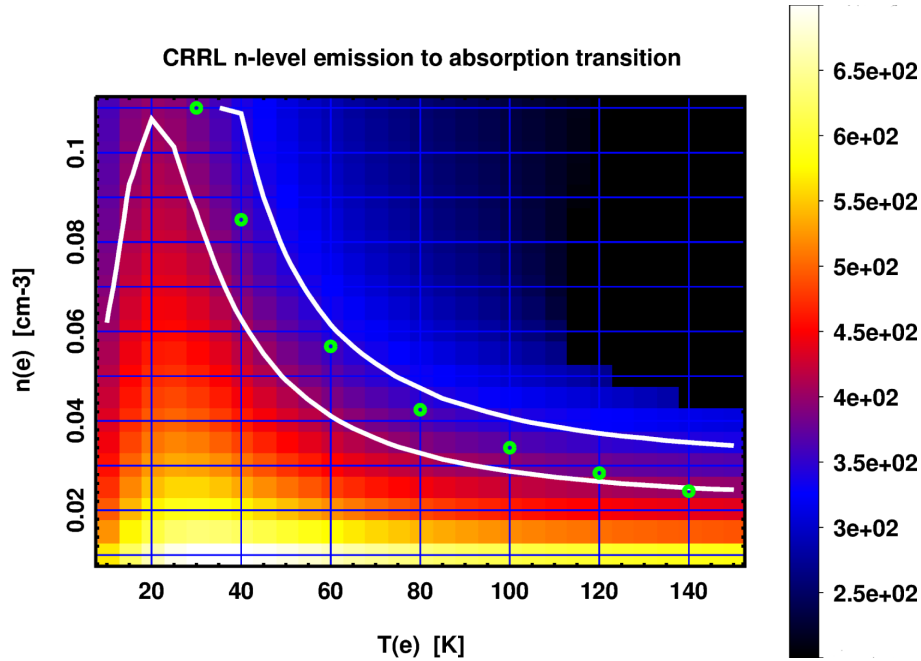


**Figure 12.** CRRL  $n$ -level transition value as a function of  $T_e$  and  $n_e$  for our model grid. The white contours are drawn for  $n = 340$  and  $400$ . This  $n$ -range for the transition corresponds to the range for our measurements. The green circles highlight values of constant electron pressure  $p_e = 0.04 \times 85 = 3.4 \text{ K cm}^{-3}$ . This shows that the transition  $n$ -level value is a good indicator of the electron pressure in the 20–140 K range.

### 5.1 Gas pressure

In the previous sections, we found that we can constrain the electron temperature and density for both components to better than 15 per cent. If we consider  $T_e$  and  $n_e$  to be independent variables, then this translates to an uncertainty of up to 20 per cent for the electron pressure at the  $1\sigma$  confidence level. One would expect the uncertainty on the pressure to increase at the  $2$  and  $3\sigma$  levels; however, this is not observed in Figs 8 and 9. These figures show that  $T_e$  and  $n_e$  are not independent and that the electron pressure remains to be constrained to better than 20 per cent at the  $3\sigma$  confidence level. This tight relationship between  $T_e$  and  $n_e$ , along lines of almost constant pressure, is driven primarily by our constraints on the range in  $n$  where the CRRL emission to absorption transition takes place (Fig. 12).

Although the electron pressure itself is well constrained by our measurements, there is still an uncertainty in translating this to a thermal gas pressure due to the unknown abundance of carbon in these clouds. The typical gas-phase carbon abundance in the ISM has been found to be  $[C/H] \sim 1.4 \times 10^{-4}$  (e.g. Cardelli et al. 1996). It is possible to derive the carbon abundance  $[C/H]$  by comparing CRRL measurements with H I 21-cm absorption measurements, under the assumption that the lines arise from the same gas and that within this gas singly ionized carbon is the dominant state of carbon, i.e.  $N(C\text{ II})/N(\text{H I}) \approx N(C)/N(H) = [C/H]$  (PAE89; Oonk et al. 2015).

H I 21-cm absorption measurements have been carried out by, for example, Mebold & Hills (1975), Bieging et al. (1991) and Schwarz et al. (1997). These studies find three main H I-absorbing components at  $-47$ ,  $-38$  and  $0 \text{ km s}^{-1}$ . These H I 21-cm components, in terms of velocity and FWHM, are in good agreement with our CRRL measurements and indicate that it is likely that the H I 21-cm absorption and our CRRL measurements spatially trace the same gas structures. A similar conclusion was reached by KAP98 (and refer-

ences therein). However, these studies also find that the H I 21-cm absorption measurements are heavily saturated for the  $-47 \text{ km s}^{-1}$  component and mildly saturated for the  $-38 \text{ km s}^{-1}$  component. This means that from these measurements we can obtain only a lower limit to true cold H I column density. Following Schwarz et al. (1997), we find  $N(\text{H I}) > 4 \times 10^{21}$  and  $N(\text{H I}) > 3 \times 10^{21} \text{ cm}^{-2}$  for the  $-47$  and  $-38$  components, respectively. An upper limit to the H I column density can be obtained by considering the total hydrogen column  $N(\text{H})$  from X-ray observations. The maximum total  $N(\text{H})$  reported by Hwang & Laming (2012) is about  $3.5 \times 10^{22} \text{ cm}^{-2}$ . From these measurements, we can constrain only the carbon abundance to be in the range of  $[C/H] = 1.3 \times 10^{-4}$ – $11 \times 10^{-4}$  for the  $-47$  component and in the range of  $[C/H] = 0.7 \times 10^{-4}$ – $7.7 \times 10^{-4}$  for the  $-38$  component.

This range in  $[C/H]$  allowed by the RRL and H I measurements is large, and especially, the upper limits of this range are likely not realistic. We therefore adopt the gas-phase abundance by Cardelli et al. (1996) here and then we find a thermal pressure  $p_{\text{thermal}}/k = 2.4 \times 10^4 \text{ K cm}^{-3}$ . This is consistent with the model prediction of  $p_{\text{thermal}}/k \sim 1 \times 10^4 \text{ K cm}^{-3}$  by Wolfire et al. (2003, their fig. 7) for densities  $n_{\text{H}} \sim 286 \text{ cm}^{-3}$  at a Galactocentric radius of about 10.5 kpc. It is also consistent with measurements and simulations of the external pressure for molecular clouds in the Galactic mid-plane (e.g. Blitz & Thaddeus 1980; Heyer et al. 2001; Girichidis et al. 2016).

The turbulent pressure in the gas can be obtained from the observed FWHM of the turbulent (Doppler) line broadening. We calculate the turbulent velocity dispersion as  $\sigma_{\text{turbulent}} = 3^{0.5} \times \text{FWHM}/2.355$ , and find  $p_{\text{turbulent}}/k = 1.9 \times 10^5 \text{ K cm}^{-3}$  for the  $-47$  component and  $7.6 \times 10^5 \text{ K cm}^{-3}$  for the  $-38$  component. We thus find that the turbulent pressure dominates over the thermal pressure in both clouds, as is typical in the ISM of the Milky Way (e.g. Wolfire et al. 2003, and references therein).



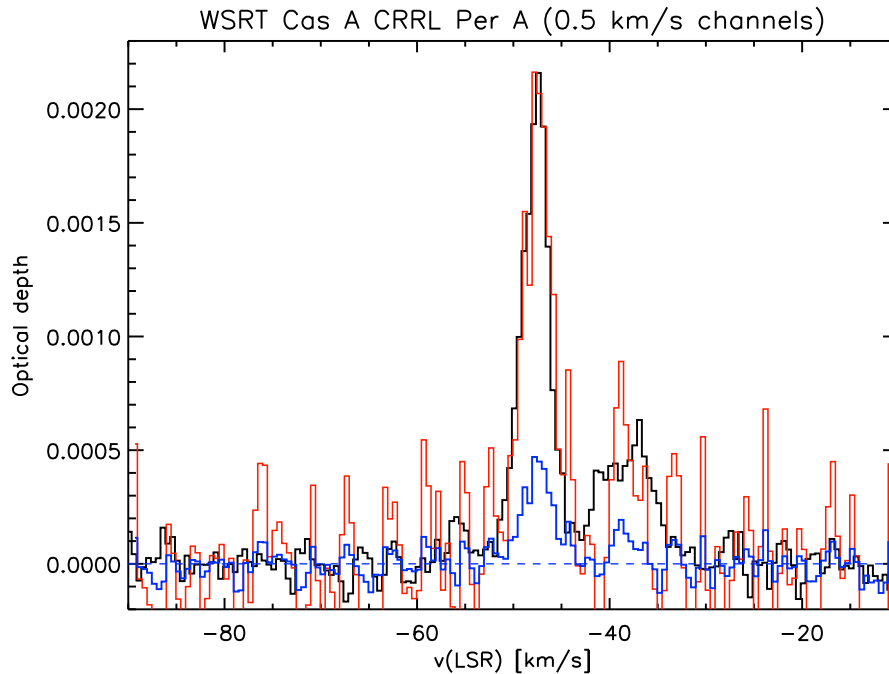


**Figure 13.** Stacked WSRT *P*-band spectrum. The spectrum shows the CRRLs (black) and HRRLs (blue) overlaid. The HRRL spectrum is shifted by  $-149.4 \text{ km s}^{-1}$  to match the CRRL spectrum. This difference corresponds to the difference in rest frequencies for the HRRLs and CRRLs. In addition, we show in red the HRRL spectrum scaled by a factor of 4.6 to match the CRRL and HRRL peaks for the  $-47$  component.

Another contribution to the pressure in the clouds comes from magnetic fields. Using OH measurements, Heiles & Stevens (1986) infer an average magnetic field strength  $B \sim 8 \mu\text{G}$ . H I 21-cm Zeeman splitting measurements by Schwarz et al. (1986) indicate an average parallel component of the magnetic field  $B_{\parallel} \sim 20 \mu\text{G}$ . The reason for the difference between these measurements is not clear. This range in measurements indicates a magnetic field pressure  $p_{\text{magnetic}}/k = (1.8\text{--}4.5) \times 10^4 \text{ K cm}^{-3}$ . This shows that the magnetic field pressure is of the same order as the thermal pressure but less than the turbulent pressure, although the H I measurements do allow for higher magnetic field pressures which may rival the turbulent pressure.

## 5.2 Hydrogen RRLs

We have detected two HRRLs in our stacked WSRT spectrum (see Fig. 3). This is the second detection of HRRLs along this line of sight. The first detection of HRRL emission at  $n = 250$  and associated with the  $-47$  component was made by SS10 at 420 MHz. Our  $n = 267$  detection of this component at 344 MHz agrees well with theirs. For the  $-38$  component, SS10 do not claim a detection, but they do see a feature in their spectrum. We confirm this feature here at the  $4\sigma$  level. The main peak of our  $-38$  HRRL agrees well with the feature seen in the spectrum by SS10; however, we do find that our line is narrower than theirs. Our  $-47$  HRRL is also narrower than the detection reported by SS10 but not as much as for the  $-38$  component. The line broadening of RRLs typically increases with increasing  $n$ , as discussed above, and this therefore does not explain the difference. The difference between our spectrum and SS10's spectrum is close to the noise level of the SS10 spectrum, and their broader feature may be caused by a noise peak. Deeper observations are necessary to investigate this further.

The HRRL velocity centroids in our WSRT spectrum, in the rest frame for hydrogen, are at  $-47.4$  and  $-38.6 \text{ km s}^{-1}$ . This agrees very well with the corresponding CRRLs and shows that both the carbon and hydrogen lines likely originate in the same clouds (see Fig. 13). The linewidth of the CRRLs and HRRLs agrees well for the  $-47$  component, but the same is not true for the  $-38$  component, where our HRRL feature is significantly narrower than the corresponding CRRL feature (Fig. 13). This could indicate that only part of the  $-38$  CRRL-emitting gas is traced by the corresponding HRRL.

### 5.2.1 Gas ionization

Low-frequency HRRLs can be used to trace the hydrogen ionization rates in the CRRL-emitting clouds, if they trace the same gas. For the  $-47$  component, this is possible, and two methods have been proposed to derive the total hydrogen ionization rate from HRRL measurements. The first method, proposed by Shaver (1976a), uses the ratio between the H I 21-cm and the HRRL integrated optical depths. It is important to use the integrated and not the peak optical depths here as the HRRL emission at sufficiently low frequencies can be affected by line broadening due to the Stark effect (Shaver 1975; S16b). In the previous section, we saw that the H I 21-cm absorption measurements are saturated and thus underestimate the true H I optical depth. This method therefore provides only an upper limit to the ionization rate  $\zeta_{\text{H}}(-47) < 5 \times 10^{-17} \text{ s}^{-1}$ .

A second method to obtain  $\zeta_{\text{H}}$  was first proposed by Sorochenko & Smirnov (1987), later modified by Sorochenko & Smirnov (1990) and SS10, and uses the ratio between the CRRL and the HRRL integrated optical depths. For convenience, we repeat the equation here:

$$\zeta_{\text{H}} = \alpha_{\text{H}}^{(2)} [\text{C}/\text{H}] \left( \frac{\tau_{\text{H}_n} \Delta \nu_{\text{H}_n}}{\tau_{\text{C}_n} \Delta \nu_{\text{C}_n}} \right) \left( \frac{\Phi_{2n\text{e}}}{T_{\text{e}}^{0.5}} \right) \left( \frac{(b_n \beta_n)_{\text{C}}}{(b_n \beta_n)_{\text{H}}} \right). \quad (1)$$



Here we have reformulated it in terms of the hydrogen (gas-phase) recombination coefficient  $\alpha^{(2)} = \alpha_{\text{H}}^{(2)} \Phi_2 T_e^{-0.5}$ , where captures to the  $n = 1$  level are excluded (Spitzer 1982).  $\alpha_{\text{H}}^{(2)} = 2.06 \times 10^{-11}$  and  $\Phi_2$  is an integral over Gaunt factors, which is tabulated in table 5.2 of Spitzer (1982). We use the  $b_n$  and  $\beta_n$  values from S16a. For the gas-phase abundance of carbon, we find that  $\zeta_{\text{H}}(-47) = 3 \times 10^{-18} \text{ s}^{-1}$ . Following PAE89, we can also use the ratio of the HRRL to CRRL optical depth to estimate the volume density ratio of ionized carbon to protons ( $n_{\text{C II}}/n_{\text{p}}$ ) and electrons ( $n_{\text{C II}}/n_{\text{e}}$ ). Using our WSRT measurements at  $n = 267$  and the  $b_n$ ,  $\beta_n$  values from S16a, we find  $n_{\text{C II}}/n_{\text{p}} = 15.5$  and  $n_{\text{C II}}/n_{\text{e}} = 0.94$ . This shows that 94 per cent of the free electrons are donated by carbon and that the proton-to-electron ratio is  $n_{\text{p}}/n_{\text{e}} = 0.06$ .

The HRRL to CRRL hydrogen ionization rate we derive for the  $-47$  component is an order of magnitude lower than reported by SS10. We find that this is entirely due to a difference in models used to compute the departure coefficients. We have also computed  $\zeta_{\text{H}}(-47)$  from their  $n = 250$  measurement using our models and find that it is consistent with our measurement at  $n = 267$ .

Our hydrogen ionization rate for the  $-47$  component is a factor of a few lower than the modelled cosmic-ray ionization rate ( $\zeta_{\text{CR}, 10\text{kpc}} \sim 1 \times 10^{-17} \text{ s}^{-1}$ ) and the extreme-UV plus X-ray ionization rate ( $\zeta_{\text{XR}, 10\text{kpc}} \sim 8 \times 10^{-18} \text{ s}^{-1}$ ) at a Galactocentric radius  $R_{\text{c}} = 10 \text{ kpc}$  (Wolfire et al. 2003). Recent measurements of the cosmic-ray ionization rate in diffuse clouds, through  $\text{H}_3^+$  observations, by Indriolo & McCall (2012) have shown that the cosmic-ray ionization rate is higher by almost an order of magnitude (i.e.  $\zeta_{\text{CR}} \sim 10^{-16} - 10^{-15} \text{ s}^{-1}$ ) for total hydrogen column densities  $N_{\text{H}} \leq 10^{22} \text{ cm}^{-2}$ . This would be inconsistent with our measurement. However, Indriolo et al. made only a few measurements in the range of  $l = 90^\circ - 130^\circ$ , most of which are upper limits, and for  $N_{\text{H}} > 2 \times 10^{22} \text{ cm}^{-2}$ , they find a steep drop to about  $2 \times 10^{-17} \text{ s}^{-1}$  for the cosmic-ray ionization rate.

### 5.2.2 Grain neutralization

Liszt (2003) has pointed out that interactions with small grains may lower the RRL-derived ionization rates. In this case, our RRL measurement would provide a firm lower limit to the actual ionization rate. Atomic ions cannot just be neutralized through gas-phase recombination, but gas-grain interactions may also play a role through a process best called mutual neutralization (e.g. Draine & Sutin 1987; Lepp & Dalgarno 1988; Lepp et al. 1988; Liszt 2003; Wolfire et al. 2008). In the literature, this process is sometimes also referred to as grain neutralization. In this process, large molecules and very small grains, or polycyclic aromatic hydrocarbons (PAHs), can become negative charged by acquiring (free) electrons (Bakes & Tielens 1994). The models by Liszt (2003) show that mutual neutralization becomes increasingly important for regions which are more heavily shielded. At the gas density observed here, these models show that, for the case of depleted gas-phase abundances ( $[\text{C}/\text{H}] = 1.4 \times 10^{-4}$ ), mutual neutralization can decrease the proton density by up to a factor of  $\sim 100$  relative to gas-phase recombination. While this process will affect the neutral atomic carbon abundance (Bakes & Tielens 1998),  $\text{C}^+$  remains the main reservoir of carbon and the dominant free-electron donor, and Liszt (2003) show that at these gas densities the free-electron density is very close to the singly ionized carbon density.

In equation (1), only gas-phase recombination is taken into account (e.g. Sorochenko & Smirnov 1987). Below we have modified

this equation by specifically including a factor  $\eta_{\text{GN}}$ , which is the ratio of the total (gas and grain) recombination rate to the gas-phase recombination rate (i.e. this is the inverse of value plotted in fig. 1 of Liszt 2003):

$$\zeta_{\text{H}} = \eta_{\text{GN}} \alpha_{\text{H}}^{(2)} [\text{C}/\text{H}] \left( \frac{\tau_{\text{H II}} \Delta \nu_{\text{H II}}}{\tau_{\text{C II}} \Delta \nu_{\text{C II}}} \right) \left( \frac{\Phi_2 n_{\text{e}}}{T_e^{0.5}} \right) \left( \frac{(b_n \beta_n)_{\text{C}}}{(b_n \beta_n)_{\text{H}}} \right). \quad (2)$$

We find that upon including grain neutralization the above hydrogen ionization rate, as derived from the HRRL-to-CRRL ratio, may need to be corrected upwards to a maximum of  $\zeta_{\text{H}}(-47) \sim 3 \times 10^{-16} \text{ s}^{-1}$ , if this process dominates within the environment in which the RRL emission arises. Similarly, the upper limit on  $\zeta_{\text{H}}(-47)$  derived from the HRRL-to-H I 21-cm ratio would also have to be corrected upwards. Currently, there are no direct observational constraints on the importance of mutual neutralization for the clouds studied here.

### 5.2.3 HRRL versus CRRL gas conditions

In the above calculations for the hydrogen ionization rate, we have implicitly assumed that the CRRLs and HRRLs trace gas with the same physical conditions and the same geometry. To test this, we plot in Fig. 14 the HRRL optical depth as a function of  $n$  with the HRRL models from S16a for the best-fitting CRRL conditions overplotted. In order to fit the model to the data, we allow the ionized hydrogen column density  $N_{\text{H II}} = n_{\text{H II}} \times L_{\text{H II}}$  to differ from the singly ionized carbon column density  $N_{\text{C II}} = n_{\text{C II}} \times L_{\text{C II}}$ . If we demand H II and C II to follow the same geometry, i.e.  $L_{\text{H II}} = L_{\text{C II}}$ , then the HRRL-to-CRRL optical depth ratio directly traces  $n_{\text{H II}}/n_{\text{C II}}$ , i.e. the relative fraction of free electrons donated by hydrogen and carbon. In agreement with above, we find  $n_{\text{H II}}/n_{\text{C II}} = 0.06$ .

Fig. 14 shows that for the  $-47$  component the HRRL model with the best-fitting CRRL gas conditions can match the high-frequency detections by us, Oonk et al. (2015) and SS10 but not our low-frequency  $3\sigma$  LBA HRRL limits. This indicates that for the  $-47$  component the CRRL and HRRL do not trace the same gas. To determine whether any other HRRL model can fit the HRRL measurements, we ran a full HRRL grid search with the same parameters as done for the CRRLs above. We constrain the model fits by demanding that the model must be able to reproduce all the detections within their  $1\sigma$  errors and provide low-frequency values which fall within the  $3\sigma$  LBA limits. For the  $-47$  component, we find that only some significantly colder and higher density models, i.e.  $T_{\text{e}} = 30 - 50 \text{ K}$ ,  $n_{\text{e}} = 0.065 - 0.11 \text{ cm}^{-3}$  and  $\text{EM}_{\text{H}} = 0.0007 - 0.002$ , are able to fit the measurements.

This comparison of the HRRL and CRRL models suggests that the HRRL and CRRL emission may not originate in the same region with the same physical conditions. Alternatively, it is possible that the CRRLs probe CO-dark molecular gas (Section 5). In such gas, carbon is ionized but hydrogen is in molecular form; a large contribution to the CRRL emission from CO-dark gas may then be expected. Spatially resolved investigations at higher frequencies (1–8 GHz) of dense PDRs have shown that in some cases narrow HRRLs and CRRLs do not trace the same gas (e.g. Roelfsema et al. 1989, and references therein). Deeper and higher spatial resolution measurements are necessary to investigate this in cold clouds at low frequencies (Salas et al., in preparation).

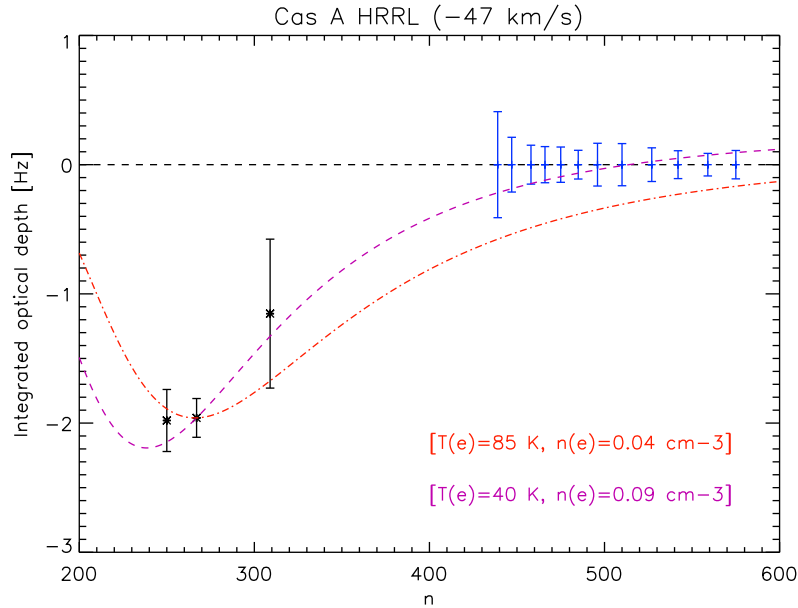


**Figure 14.** Cas A HRRL integrated optical depth versus quantum number ( $n$ ) for the  $-47 \text{ km s}^{-1}$  cloud. The three detections (black data points) are from this work, Oonk et al. (2015) and Sorochenko & Smirnov (2010). The blue bars show the  $3\sigma$  HRRL upper limits obtained from our LBA measurements (Table 6). The red curve shows the scaled HRRL model upon assuming the same physical parameters ( $T_e = 85 \text{ K}$  and  $n_e = 0.04 \text{ cm}^{-3}$ ) as the best fitting CRRL model. The scaling is done by normalizing this model at the WSRT data point and gives  $EM_H = 0.0036 \text{ cm}^{-6} \text{ pc}$ . If we set  $L_H = L_C$ , then we find  $n_{HII}/n_{CII} = 0.06$ . Alternatively,  $L_H/L_C = 0.06$  if we set  $n_{HII} = n_{CII}$ . This model does not fit the LBA upper limits. Investigating the full HRRL grid, we find that temperatures and densities in the range of  $T_e = 30\text{--}50 \text{ K}$  and  $n_e = 0.065\text{--}0.11 \text{ cm}^{-3}$ , respectively, are able to fit both the measurements and the upper limits. The purple curve shows an example with  $T_e = 40 \text{ K}$ ,  $n_e = 0.09 \text{ cm}^{-3}$  and has  $EM_H = 0.0014 \text{ cm}^{-6} \text{ pc}$ .

### 5.3 CRRL modelling uncertainties

The modelling approach which we used here has a number of uncertainties which we will discuss below.

#### 5.3.1 Spatial structure

We have used a homogeneous slab model with a constant temperature and density and a filling factor of unity to model the clouds in front of Cas A. This approach is likely a simplification of the true situation for these clouds. There have been a number of studies performed to explore the physical conditions and spatial structure in the cool atomic and molecular gas of the Cas A clouds (e.g. de Jager et al. 1978; Batrla et al. 1983, 1984; Bieging et al. 1991; Anantharamaiah et al. 1994; Schwarz et al. 1997; Liszt & Lucas 1999; Mookerjee et al. 2006; Kilpatrick et al. 2014). These studies show (i) that the cool gas extends over most of the face of the remnant, (ii) that the cool gas has spatial structure on arcmin-scales and peaks in a filamentary-like structure over the southern part of the remnant running from the western hotspot to the south-east of the remnant, and (iii) that the  $-38$  component is more localized and shifted towards the western part of the remnant, as compared to the  $-47$  component, although this could be a sensitivity issue. The observed CRRL emission is consistent with this arcmin-scale picture, and Anantharamaiah et al. (1994) argue that on  $2.7 \times 2.4 \text{ arcmin}^2$  scales the CRRL emission shows a better spatial and velocity correlation with H I 21-cm absorption than with  $^{12}\text{CO}$  emission, although they also note that there are differences between all three tracers.

Observations of  $^{12}\text{CO}$  on larger scales show that the southern filamentary structure seen in absorption against Cas A is likely the edge of a larger molecular cloud complex which is located to the south of the remnant (e.g. Batrla et al. 1984; Kilpatrick et al. 2014). Higher

spatial resolution studies have been performed in H I 21-cm absorption and in several molecular tracers (e.g. Batrla et al. 1983, 1984; Bieging et al. 1991). The H I 21-cm study by Bieging et al. (1991), with a spatial resolution of 7 arcsec, shows that the H I absorption extends over the entire face remnant and that there is great complexity within it. They find several morphological structures identified based on velocity cuts and describe these structures as filaments, arcs, loops and irregulars with typical sizes varying from about 0.5 to 3 arcmin. Molecular absorption line studies are consistent with these sizes. Additional substructure may be present, and Batrla et al. (1984) based on the low filling factor ( $f = 0.04$ ) they derive for one of their ammonia clouds find that the molecular clouds may contain structure as small as 8 arcsec. They interpret this as evidence for dense, high-pressure clumps with physical sizes of 0.12 pc and pressures  $p_{\text{thermal}}/k \sim 7 \times 10^4 \text{ K cm}^{-3}$ .

Given the available data, we recognize that our CRRL measurements likely measure an average which is weighted towards the southern part of the remnant. By assuming a unity filling factor, we average over a range in physical conditions which may be present in the gas. On arcmin-scales, the total, i.e. the sum of the  $-38$  and  $-47$  components, CRRL optical depth does not vary by more than about a factor of 2 across the remnant (Anantharamaiah et al. 1994). Asgekar et al. (2013) show that, except for an overall increase in optical depth, there are no significant differences for the total CRRL integrated optical depth as a function of  $n$  (albeit over a very limited range in  $n$ ) observed against the western hotspot as compared to the sum over the entire remnant.

The low-frequency CRRLs observed here likely trace the gas intermediate between the atomic and molecular phases (e.g. Section 5), and a substantial filling factor seems reasonable. Low filling factors for the CRRL-emitting gas would imply even larger, and likely unrealistic, C II column densities, given the required

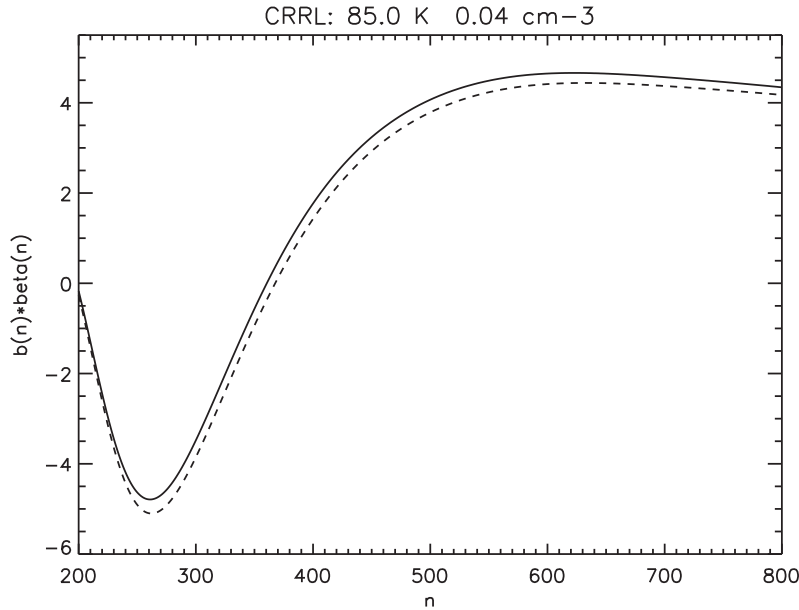


**Figure 15.** Comparison of the  $b_n\beta_n$  values for the ratio  $R$  of the  $^2P_{3/2}$  over the  $^2P_{1/2}$  population of carbon. The solid line gives the  $b_n\beta_n$  value for S16a models which do not include collisions with molecular hydrogen. The dashed line gives the  $b_n\beta_n$  value for S16a models which do include collisions with molecular hydrogen. Here, we have used  $T_e = 85$  K,  $n_e = 0.04$  cm $^{-3}$ ,  $n_{H_2} = n_{H_I}$  and the collision rates from Tielens & Hollenbach (1985).

beam dilution corrections. The physical conditions derived here may therefore represent a reasonable average of the true physical conditions. If higher spatial resolution observations find evidence for low filling factors of the CRRL-emitting gas, then this can affect the observed optical depths as a function of  $n$  as the underlying continuum emission from Cas A is also highly structured in terms of the surface brightness and spectral index (e.g. Kassim et al. 1995). In particular, this may affect the measurements for the potentially more localized  $-38$  component. A more detailed analysis of the spatial structure for the CRRLs along the line of sight to Cas A will be presented elsewhere (Salas et al., in preparation).

### 5.3.2 Radiation field and radiative transfer

In this work, we have assumed that the clouds are embedded within an isotropic radiation field. At the distance of Cas A, an angular scale of 1 arcmin corresponds to 1 pc. Over these small spatial scales, we feel it is reasonable to expect that the low-frequency Milky Way synchrotron radiation field is isotropic. Comparison of our LOFAR interferometric data with existing single-dish radio surveys (e.g. Landecker & Wielebinski 1970; Haslam et al. 1982; Roger et al. 1999) shows that the bulk ( $\gtrsim 80$  per cent) of the low-frequency Milky Way synchrotron emission is emitted on scales larger than about 10 wavelengths, or equivalently on angular scales larger than about  $6^\circ$ . The existing low-frequency Milky Way single-dish measurements do not allow for a diffuse Milky Way contribution which is less than about 800 K at 100 MHz (e.g. Landecker & Wielebinski 1970; Haslam et al. 1982; Roger et al. 1999), and our measured linewidths do not allow for a total contribution greater than about 1600 K at 100 MHz. Given the above constraints, we have investigated lowering the Milky Way contribution and adding a contribution from Cas A to the radiation field. For the data presented here, we find that this does not provide a better fit.

As discussed in S16b, the equations used here to calculate the linewidths and optical depths are approximations. These approximations are valid at sufficiently high  $n$  levels. This is especially true in the case of a bright background source such as Cas A. Following the prescription in S16b, we have, for a few representative cases, calculated the exact solutions to the radiative transfer equation for the CRRLs along the line of sight to Cas A. We find that the differences between the approximate and exact solutions in the case of Cas A are less than 1 per cent for  $n > 225$  and as such do not affect our results.

### 5.3.3 Collision rates

Our CRRL models depend on the ratio of the  $^2P_{3/2}$  to the  $^2P_{1/2}$  population, also referred to as the  $R$  value (Walmsley & Watson 1982; Ponomarev & Sorochenko 1992). We have used the formulation by S16a, who give  $R$  in terms of collisions with electrons and hydrogen atoms using the rates given in Tielens & Hollenbach (1985) and Launay & Roueff (1977). The S16a model does not include collisions with molecular hydrogen. We have investigated adding these collisions, using the rate given in Tielens & Hollenbach (1985), and we find a small systematic effect on the computed  $b_n\beta_n$  values, which are shifted by about 5 per cent, for  $n_{H_2} = n_{H_I}$ , towards lower values upon including these collisions (see Fig. 15).

A more important effect on the CRRL models, in terms of  $b_n\beta_n$ , is the choice in  $\ell$ -changing collisions. S16a uses rates by Vranceanu, Onofrio & Sadeghpour (2012). These rates were the most up to date rates for the  $\ell$ -changing collisions at the time of writing. S16a also investigated rates by Pengelly & Seaton (1964). These rates give a qualitatively similar  $b_n\beta_n$  behaviour, but quantitatively the results can differ substantially. The Pengelly & Seaton (1964) rates are not suitable for this work as they diverge for densities  $n_e < 0.05$  cm $^{-3}$ . Very recently there has been renewed interest in these rates by

Guzman et al. (2016, 2017). In a future paper, we will address the influence of the  $\ell$ -changing rates on the Cas A clouds in more detail.

## 6 CONCLUSIONS

In this paper, we present the first results from our ongoing LCASS radio survey of the cold ISM along the line of sight to Cas A. We have obtained high signal-to-noise ratio observations with LOFAR in the range of 33–78 MHz and complemented these with WSRT observations in the range of 304–386 MHz. The high signal-to-noise ratio and high spectral resolution CRRL spectra allow us to carry out a detailed velocity resolved study of the foreground cold clouds in the Perseus arm at  $-47$  and  $-38$  km s $^{-1}$ . We have used our new CRRL models (S16a; S16b) to interpret the dependence of CRRL linewidth and integrated optical depth on quantum number  $n$ . For the first time, we have found a set of physical parameters which can describe both the linewidth and integrated optical depth.

(i) The CRRL linewidth and optical depths for the  $-47$  and the  $-38$  components can be modelled as two uniform clouds. The best-fitting model for the  $-47$  km s $^{-1}$  cloud has  $T_e(-47) = 85 \pm 5$  K,  $n_e(-47) = 0.040 \pm 0.005$  cm $^{-3}$ ,  $L_{CII} = 35.3 \pm 1.2$  pc and  $T_{R,100} = 1351 \pm 81$  K. The best-fitting model for the  $-38$  km s $^{-1}$  cloud has  $T_e(-38) = 85 \pm 10$  K and  $n_e(-38) = 0.040 \pm 0.005$  cm $^{-3}$ ,  $L_{CII} = 18.6 \pm 1.6$  pc and  $T_{R,100} = 1507 \pm 128$  K. The  $-38$  km s $^{-1}$  cloud has a steeper increase in optical depth at low frequencies, as compared to the  $-47$  km s $^{-1}$  cloud, and is fitted less well by our models. Together with the broad line profile, this may indicate that the  $-38$  km s $^{-1}$  cloud consists of multiple velocity components with potentially different physical conditions.

(ii) The derived C II column density is  $(4.4 \pm 0.6) \times 10^{18}$  and  $(2.3 \pm 0.3) \times 10^{18}$  cm $^{-2}$  for the  $-47$  and  $-38$  km s $^{-1}$  clouds, respectively. This is higher than in previous investigations as our  $b_n \times \beta_n$  values for carbon from the S16a models are significantly lower than in previous models (e.g. Walmsley & Watson 1982; Ponomarev & Soroichenko 1992). The large path-lengths inferred from these C II column densities indicate that likely we are viewing sheet-like structures.

(iii) The electron pressure, even for the lower signal-to-noise ratio measurements of the  $-38$  km s $^{-1}$  cloud, is determined to better than 20 per cent uncertainty out to the  $3\sigma$  confidence level. The resulting thermal hydrogen pressure is  $(2.4 \pm 0.5) \times 10^4$  K cm $^{-3}$ , if we assume the gas-phase abundance of carbon. This pressure is high but consistent with our expectations of dense clouds in the Galactic mid-plane at a Galactocentric radius of about 10.5 kpc.

(iv) The detection of HRRLs with the WSRT allows us to assess that the ionized hydrogen-to-carbon ratio is about 0.06. This means that 94 per cent of the free electrons are donated by carbon. The corresponding hydrogen ionization rate would be  $(3 \pm 0.05) \times 10^{-18}$  s $^{-1}$  if the HRRL and CRRL trace the same gas. Our models indicate that this is not likely and much of the CRRL emission may be associated with CO-dark molecular gas. Deeper and higher spatial resolution measurements are necessary to investigate this further.

From our measurements and model, we find a consistent picture for the  $-47$  and  $-38$  clouds in the Perseus arm towards Cas A, in that they are dense, cool clouds with very low hydrogen ionization levels. The saturated H I 21-cm absorption measurements prevent us from determining the carbon to hydrogen abundance for these clouds. Here, we have used the gas-phase abundance of carbon (i.e.  $[C/H] = 1.4 \times 10^{-4}$ ) to convert our carbon measurements to

hydrogen measurements. We find high thermal pressures and high hydrogen column densities ( $N_H \sim 10^{22}$  cm $^{-2}$ ).

For these conditions, we may be tracing the atomic to molecular hydrogen interface, and the gas cooling of such a cloud will be dominated by the [C II] 158  $\mu$ m line (Wolfire et al. 2003, their Fig. 10). S16b shows that the [C II] 158  $\mu$ m line can provide an independent constraint on the temperature if it traces the same gas as the CRRLs.

The work presented here shows that we can use low-frequency CRRLs to accurately determine the physical conditions of cold neutral clouds in the ISM. Future observations with LOFAR using LBA and also the High Band Antennas will allow us to determine this for many other cold clouds making up the CNM and thus assess their role within the ISM and their relationship with molecular gas. The CRRL models used here do contain some systematic uncertainties, in particular concerning the  $\ell$ -changing collisions. We will investigate the effects of some very recent updates of these rates by Guzman et al. (2016, 2017) in a future paper.

## ACKNOWLEDGEMENTS

LOFAR, designed and constructed by ASTRON, has facilities in several countries, which are owned by various parties (each with their own funding sources) and collectively operated by the International LOFAR Telescope (ILT) foundation under a joint scientific policy

The authors would like to thank the LOFAR and WSRT observatory staff for their assistance in obtaining and handling of this large data set. The LOFAR observations presented here are taken as part of LCASS. We gratefully acknowledge that LCASS is carried out using Director's Discretionary Time under project DDT001. We are grateful to the referee Malcolm Walmsley for his very helpful and constructive review.

JBRO, AGGMT, HJAR and PS acknowledge financial support from the NWO Top LOFAR-CRRL project, project No. 614.001.351. RJvW is supported by a Clay Fellowship awarded by the Harvard-Smithsonian Center for Astrophysics. AGGMT acknowledges support through the Spinoza premie of the Dutch Science Organization (NWO).

## REFERENCES

- Anantharamaiah K. R., Erickson W. C., Payne H. E., Kantharia Nimisha G., 1994, ApJ, 430, 682
- Andersson B. G., Roger R. S., Wannier P. G., 1992, A&A, 260, 355
- Asgekar A. et al., 2013, A&A, 551, L11
- Baars J. W. M., Mezger P. G., Wendker H., 1965, ApJ, 142, 122
- Bakes E. L. O., Tielens A. G. G. M., 1994, ApJ, 427, 822
- Bakes E. L. O., Tielens A. G. G. M., 1998, ApJ, 499, 258
- Batrla W., Wilson T. L., Martin-Pintado J., 1983, A&A, 119, 139
- Batrla W., Walmsley C. M., Wilson T. L., 1984, A&A, 136, 127
- Bieging J. H., Crutcher R. M., 1986, ApJ, 310, 853
- Bieging J. H., Goss W. M., Wilcots E. M., 1991, ApJS, 75, 999
- Blake D. H., Crutcher R. M., Watson W. D., 1980, Nature, 287, 707
- Blitz L., Thaddeus P., 1980, ApJ, 241, 676
- Bridle A. H., Purton C. R., 1968, AJ, 73, 717
- Briggs D. S., 1995, PhD thesis, New Mexico Institute of Mining Technology
- Brocklehurst M., 1970, MNRAS, 148, 417
- Brocklehurst M., Salem M., 1977, Comput. Phys. Commun., 13, 39
- Brocklehurst M., Seaton M. J., 1972, MNRAS, 157 179
- Cardelli J. A., Meyer D. M., Jura M., Savage B. D., 1996, ApJ 467 334
- de Jager G., Graham D. A., Wielebinski R., Booth R. S., Gruber G. M., 1978, A&A, 64, 17
- Dickey J. M., Benson J. M., 1982, AJ, 87, 2



- Dickey J. M., Lockman F. J., 1990, *ARA&A*, 28, 215
- Draine B. T., Sutin B., 1987, *ApJ*, 320, 803
- Dupree A. K., 1969, *ApJ*, 158, 491
- Dupree A. K., 1971, *ApJ*, 170, L119
- Erickson W. C., McConnell D., Anantharamaiah K. R., 1995, *ApJ*, 454, 125
- Girichidis P. et al., 2016, *MNRAS*, 456, 3432
- Golynkin A. A., Konovalenko A. A., 1991a, *Sov. Astron. Lett.*, 17, 7
- Golynkin A. A., Konovalenko A. A., 1991b, *Sov. Astron. Lett.*, 17, 10
- Gordon M. A., Sorochenko R. L., 2009, *Radio Recombination Lines: Their Physics and Astronomical Applications*. Springer Science+Business Media, New York
- Guzman F., Badnell N. R., Williams R. J. R., van Hoof P. A. M., Chatzikos M., Ferland G. J., 2016, *MNRAS*, 459, 3498
- Guzman F., Badnell N. R., Williams R. J. R., van Hoof P. A. M., Chatzikos M., Ferland G. J., 2017, *MNRAS*, 464, 312
- Haslam C. G. T., Salter C. J., Stoffel H., Wilson W. E., 1982, *A&AS*, 47, 1
- Heiles C., 1984, *ApJS*, 55, 585
- Heiles C., Stevens M., 1986, *ApJ*, 301, 331
- Heiles C., Troland T. H., 2003, *ApJ*, 586, 1067
- Heyer M. H., Carpenter J. M., Snell R. L., 2001, *ApJ*, 551, 852
- Hwang U., Laming J. M., 2012, *ApJ*, 746, 130
- Indriolo N., McCall B. J., 2012, *ApJ*, 745, 91
- Jenkins E. B., Tripp T. M., 2011, *ApJ*, 734, 65
- Kantharia N. G., Anantharamaiah K. R., 2001, *JA&A*, 22, 51
- Kantharia N. G., Anantharamaiah K. R., Payne H. E., 1998a, *ApJ*, 506, 758 (KAP98)
- Kantharia N. G., Anantharamaiah K. R., Goss W. M., 1998b, *ApJ*, 504, 375
- Kassim N. E., Perley R. A., Dwarakanath K. S., Erickson W. C., 1995, *ApJ*, 455, L59
- Kilpatrick C. D., Bieging J. H., Rieke G. H., 2014, *ApJ*, 796, 144
- Konovalenko A. A., Sodin L. G., 1980, *Nature*, 283, 360
- Konovalenko A. A., Stepkin S. V., 2005, *EAS Pub. Ser.*, 15, 271
- Landecker T. L., Wielebinski R., 1970, *Aust. J. Phys. Suppl.*, 16, 1
- Launay J.-M., Roueff E., 1977, *J. Phys. B: At. Mol. Phys.*, 10, 879
- Lepp S., Dalgarno A., 1988, *ApJ*, 335, 769
- Lepp S., Dalgarno A., van Dishoeck E. F., Black J. H., 1988, *ApJ*, 329, 418
- Liszt H., 2003, *A&A*, 398, 621
- Liszt H., Lucas R., 1999, *A&A*, 347, 258
- McKean J. P. et al., 2016, *MNRAS*, 463, 3143
- McMullin J. P., Waters B., Schiebel D., Young W., Golap K., 2007, in Shaw R. A., Hill F., Bell D. J., eds, *ASP Conf. Ser. Vol. 376, Astronomical Data Analysis Software and Systems XVI*. Astron. Soc. Pac., San Francisco, p. 127
- Mebold U., Hills D. L., 1975, *A&A*, 42, 187
- Mookerjee B., Kantharia N. G., Roshni D. A., Masur M., 2006, *MNRAS*, 371, 761
- Natta A., Walmsley C. M., Tielens A. G. G. M., 1994, *ApJ*, 428, 209
- Offringa A. R., de Bruyn A. G., Biehl M., Zaroubi S., Bernardi G., Pandey V. N., 2010, *MNRAS*, 405, 155
- Oonk J. B. R. et al., 2014, *MNRAS*, 437, 3506
- Oonk J. B. R., Morabito L. K., Salgado F., Toribio M. C., van Weeren R. J., Tielens A. G. G. M., Rottgering H. J. A., 2015, in *Proc. Sci., The Physics of the Cold Neutral Medium: Low-frequency Radio Recombination Lines with the Square Kilometre Array*. SISSA, Trieste, PoS(AASKA14)139
- Palmer P., 1967, *ApJ*, 149, 715
- Pandey V. N., van Zwieten J. E., de Bruyn A. G., Nijboer R., 2009, in Saikia D. J., Green D. A., Gupta Y., Venturi T., eds, *ASP Conf. Ser. Vol. 407, Calibrating LOFAR Using the Black Board Selfcal System*. Astron. Soc. Pac., San Francisco, p. 384
- Parker E. A., 1968, *MNRAS*, 138, 407
- Payne H. E., Anantharamaiah K. R., Erickson W. C., 1989, *ApJ*, 341, 890 (PAE89)
- Payne H. E., Anantharamaiah K. R., Erickson W. C., 1994, *ApJ*, 430, 690
- Pengelly R. M., Seaton M. J., 1964, *MNRAS*, 127, 165
- Ponomarev V. O., Sorochenko R. L., 1992, *Sov. Astron. Lett.*, 18, 215
- Roelfsema P. R., Goss W. M., Geballe T. R., A&A, 222, 247
- Roger R. S., Costain C. H., Landecker T. L., Swerdlyk C. M., 1999, *A&AS*, 137, 7
- Salgado F., Morabito L. K., Oonk J. B. R., Salas P., Toribio M. C., Röttgering H. J. A., Tielens A. G. G. M., 2016a, preprint ([arXiv:1609.06938](https://arxiv.org/abs/1609.06938)) (S16a)
- Salgado F., Morabito L. K., Oonk J. B. R., Salas P., Toribio M. C., Röttgering H. J. A., Tielens A. G. G. M., 2016b, preprint ([arXiv:1609.07159](https://arxiv.org/abs/1609.07159)) (S16b)
- Sancisi R., Goss W. M., Anderson C., Johansson L. E. B., Winnberg A., 1974, *A&A*, 35, 445
- Schwarz U. J., Troland T. H., Albinson J. S., Bregman J. D., Goss W. M., Heiles C., 1986, *ApJ*, 301, 320
- Schwarz U. J., Goss W. M., Kalberla P. M. W., 1997, *A&AS*, 123, 43
- Seaton M. J., 1959, *MNRAS*, 119, 81
- Shaver P. A., 1975, *Pramana*, 5, 1
- Shaver P. A., 1976a, *A&A*, 49, 1
- Shaver P. A., 1976b, *A&A*, 49, 149
- Smith R. J., Glover S. C. O., Clark P. C., Klessen R. S., Springel V., 2014, *MNRAS*, 441, 1628
- Sofia U. J., Cardelli J. A., Guerin K. P., Meyer D. M., 1997, *ApJ*, 482, L105
- Sorochenko R. L., Smirnov G. T., 1987, *Sov. Astron. Lett.*, 13, 77
- Sorochenko R. L., Smirnov G. T., 1990, in Gordon M. A., Sorochenko R. L., eds, *Proc. IAU Colloq. 125, 163, 189, Radio Recombination Lines: 25 Years of Investigation*. Kluwer, Dordrecht
- Sorochenko R. L., Smirnov G. T., 2010, *Astron. Rep.*, 54, 776 (SS10)
- Spitzer L., Jr 1982, *Physical Processes in the Interstellar Medium*. Wiley, New York
- Spitzer L., 1978, *Physical Processes in the Interstellar Medium*. Wiley-Interscience, New York
- Spitzer L., Jenkins E. B., 1975, *ARA&A*, 13, 133
- Stepkin S. V., Konovalenko A. A., Kantharia N. G., Udaya Shankar N., 2007, *MNRAS*, 374, 852
- Tielens A. G. G. M., Hollenbach D., 1985, *ApJ*, 291, 722
- van Dishoeck E. F., Black J. H., 1986, *ApJS*, 62, 109
- van Haarlem M. P. et al., 2013, *A&A*, 556, 2
- Viala Y. P., Roueff E., Abgrall H., 1988, *A&A*, 190, 215
- Vrinceanu D., Onofrio R., Sadeghpour H. R., 2012, *ApJ*, 747, 56
- Walmsley C. M., Watson W. D., 1982, *ApJ*, 255, L123
- Wolfire M. G., McKee C. F., Hollenbach D., Tielens A. G. G. M., 2003, *ApJ*, 587, 278
- Wolfire M. G., Tielens A. G. G. M., Hollenbach D., Kaufman M. J., 2008, *ApJ*, 680, 384
- Wyrowski F., Schilke P., Hofner P., Walmsley C. M., 1997, *ApJ*, 487, L171

This paper has been typeset from a  $\text{\LaTeX}$  file prepared by the author.